1-28-2015

Quadrupole Strong Focusing for Space-Charge Dominated Electron Beams in Traveling-Wave Tubes

Kimberley Lementino

Kimberley Eden Leslie Lementino

Canidate

Electrical and Computer Engineering

Department

This disseration is approved, and it is acceptable in quality and form for publication:

Approved by the Dissertation Committee:

Edl Schamiloglu, Chairperson

Mark Gilmore

Bruce Carlsten

Cristina Pereyra

Quadrupole Strong Focusing for Transport of Space-Charge Dominated Electron Beams in Traveling-Wave Tubes

by

Kimberley E.L. Nichols

B.A., St. John's College, 2008

DISSERTATION

Submitted in Partial Fulfillment of the
Requirements for the Degree of

Doctor of Philosophy
Engineering

The University of New Mexico

Albuquerque, New Mexico

December, 2014

Dedication

To my son, Wesley, whose patience has been my success.

To my mother, Susan, for her support.

To God who has made everything possible.

"Definiteness of purpose is the starting point of all achievement."

– W. Clement Stone

Acknowledgments

I would like to thank my advisor, Professor Edl Schamiloglu, for his support, and my co-advisor, Dr. Bruce Carlsten, for his enthusiasm and countless hours of effort. I would also like to thank Tony Byers, who always believed in me. I also send gratitude to the many people who have been my support and my friends.[1]

Financial Support provided by TechFlow Scientific, and the Air Force Research Laboratory.

[1]To my family. To Teo, Abby, Alejandro, Nat, Dorca, Aaron, and Wesley.

Quadrupole Strong Focusing for Transport of Space-Charge Dominated Electron Beams in Traveling-Wave Tubes

by

Kimberley E.L. Nichols

B.A., St. John's College, 2008

Ph.D., Engineering, University of New Mexico, 2014

Abstract

Analysis of quadrupole focusing lattices for high-frequency TWTs is presented. This work is motivated by recent work performed at the Naval Research Laboratory (NRL) which demonstrated an advantageous case for strong focusing employing a Halbach quadrupole lattice. Using realistic Permanent Magnet Quadruple (PMQ) field cancellation, the advantage of using PMQ to transport higher current densities than Permanent Periodic Magnet (PPM) lattices disappears, while other advantages for employing quadrupole focusing remain. This dissertation gives a comprehensive analysis of the applicability of PMQ focusing in vacuum electronic devices.

Contents

List of Figures

List of Figures

List of Tables

Chapter 1

Introduction

1.1 Overview

Novel millimeter–wave vacuum electronic devices (VEDs) that are useful for applications such as communications, imaging, and radar, are requiring higher performance than we currently have available to us. In particular, as we go to higher frequencies (greater than 50 GHz), it is difficult to achieve sufficient power for the desired applications. In this high-frequency regime one device of interest is the traveling-wave-tube (TWT). TWTs have demonstrated that they are robust, reliable, and have the potential to be scaled to very high frequencies. However, at these very minute dimensions there are many challenges to obtaining sufficient power. The beam voltage must be kept sufficiently low to avoid electric-field breakdown in the gun region. It is also desirable to keep the beam voltage down to maintain a portable system as these devices require modulators to drive them and high voltage modulators are heavy and bulky. In order to achieve sufficient power with such constraints on the voltage, it is desirable to increase the beam current. Quadrupole strong focusing is proposed as a potential method to transport higher current densities in these beams.

Quadrupole strong focusing has long been used to transport high energy, emittance

dominated electron beams for accelerator applications. It has not, however, been employed to transport lower energy, space-charge dominated electron beams for application to linear VEDs, such as the TWT. Previous work has suggested that there could be advantages for applying the Periodic Magnet Quadrupole (PMQ) focusing method to space-charge dominated electron beams; specifically, it has been proposed that employing a PMQ focusing scheme in lieu of traditional focusing schemes would use less magnetic material to focus and transport a comparable electron beam. In addition, the stronger focusing forces are believed to be able to transport higher current density electron beams than the traditional focusing schemes. Despite these advantages, very little work has been performed to analyze the scope of applicability of this focusing method.

The purpose of this work is to provide a thorough analysis of quadrupole strong focusing for VED applications. This study includes an analysis of the magnetic fields and magnet-magnet interactions, a thorough analysis of the beam envelope interaction with the PMQ transport lattice, an analysis of the beam dynamics for various device dimensions (scalability) as well as various beam energies, a comparison and limitation study of the traditional Periodic Permanent Magnet (PPM) focusing method, a discussion of the application of PMQ focusing to pencil and other beam geometries, and studies of emittance growth in PPM and PMQ lattices. Some results from the envelope codes can be found in [6].

1.2 Electron Beam Focusing and Transport

Linear VEDs rely on an electron beam interaction with an RF wave in which the electron beam transfers energy to the wave. This interaction requires an electron beam whose longitudinal dimension is much longer than its transverse dimensions which maintains a constant transverse cross-section. The electron beam must be confined to counteract the natural spread of the transverse beam size due to the self-repelling forces of the electrons for the length of the RF interaction circuit; this is called beam transport.

One common method for confining the beam is to apply a uniform axial magnetic field in the direction of beam propagation– any electron motion which is perpendicular to this field generates forces which confine the beam. Another common method is to use periodic focusing cells which counteract the beam spread sufficiently until the beam reaches the next focusing cell. These systems for maintaining the beam are often called beam focusing systems, or beam transport systems. The periodic systems are often called focusing or transport lattices, and the periodic cells employed are often called lenses due to the optical analog of focusing systems.

The spread of the electron beam due to the self-forces acting on each other with no constraints is called Universal Beam Spread (UBS) [7].The force due to the space–charge acting on an electron at an initial radius r_i is given by:

$$\frac{eE_s}{\gamma^2} = \frac{eI_o r_i}{2\pi\epsilon_0 c\beta\gamma^2 r^2}, \tag{1.1}$$

where e (defined as negative) is the electron charge, E_s is the electric field due to the electron Coulomb interactions, I_0 is the current of the electron beam, r_i is the initial radius of the beam, ϵ_0 is the permittivity of free space, c is the speed of light, β is the ratio of beam velocity in the inertial frame of reference to the speed of light, γ is the lorentz relativistic factor, and r is the radius of the electron beam. The effect of UBS on electron motion for an electron with initial radius r_i is graphed for a typical TWT beam in Fig. 1.1.

Since the force on the electron is proportional to its initial radius, electron paths do not cross; therefore, the evolution of the beam cross-section can be determined by following the motion of the edge electrons, and this is called the beam envelope. Then the equation of motion of the edge electron at radius r over time can be determined by

$$\frac{d^2r}{dz^2} = \frac{eI_0}{2\epsilon_0(c\beta)^3 r}, \tag{1.2}$$

or in terms of beam voltage V_0,

$$\frac{d^2r}{dz^2} = \frac{I_0}{4\sqrt{2}\pi\epsilon_0\sqrt{e/m}V_0^{3/2}r}, \tag{1.3}$$

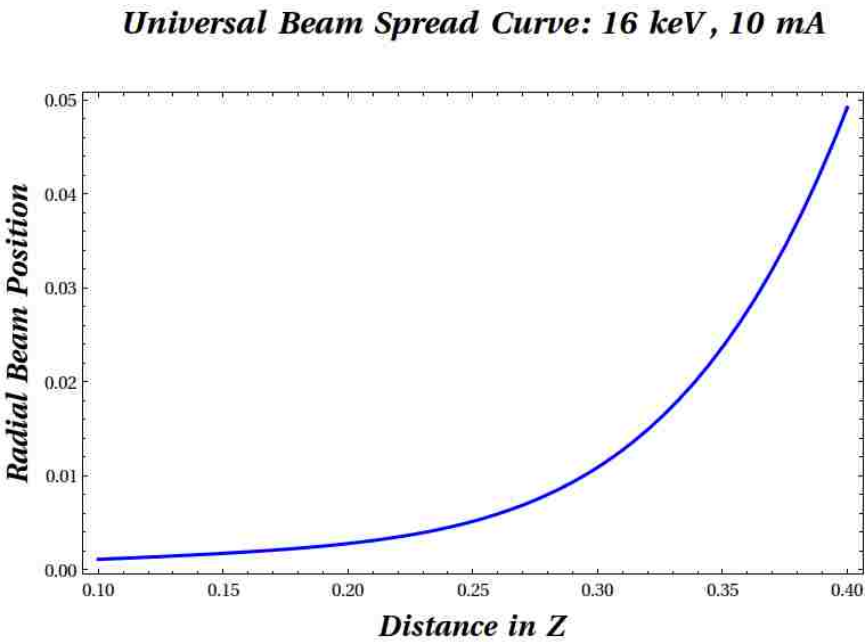

Figure 1.1: Universal beam spread or space–charge spread.

where m is the electron mass.

The forces acting on the electron beam can be clearly seen by looking at the envelope equation of the electron beam, where below we assume that the axial magnetic field on the cathode is zero:

$$r''[s] + \kappa[s] - \frac{2K_0}{r[s]^2} - \frac{\epsilon_{eff}}{r[s]^3} = 0. \tag{1.4}$$

The envelope equation represents the motion of the edge of the electron beam, or the beam "envelope", r is the radial distance to beam edge as a function of position s. In the second term, κ is the external magnetic field. In the third term, K_0 (which is defined to be > 0) represents the self–repelling forces of the electrons and is called the "space–charge" term. In the fourth term, ϵ_{eff} (which is also defined to be > 0) represents the effective beam emittance. Emittance is a measure of the beam quality and will be discussed in more detail in Chapter 5. Typically, the space–charge term dominates for electron beams in VEDs and the emittance term dominates for the higher energy beams used in accelerator applications.

To prevent the beam from spreading the second term must at least cancel out the third and fourth terms in the envelope equation. When the external magnetic field exactly cancels the space–charge forces, and the emittance term is negligible, the electron beam is said to be in Brillouin electron flow [8]. When there is an axial magnetic field on the cathode, it is called confined electron flow and the beam can transport greater current densities than can be achieved with Brillouin flow.

There are three main magnetic field configurations that will be discussed for transporting linear electron beams: solenoidal fields, PPM fields, and PMQ fields. Solenoids have the ability to produce very high fields for both Brillouin flow and confined flow. In addition, the fields are simple to design and produce. However, solenoids are rarely used for VED devices outside of the laboratory because they are heavy, bulky, and require external power and often cooling systems. As an alternative to solenoids, PPM focusing is much lighter in weight, much more compact, and does not consume power. It is now the standard method for electron beam confinement in TWTs. The third method that will be discussed is PMQ transport. PMQs have much different field profiles from PPMs and are even lighter in weight and more compact than PPMs.

1.3 Introduction to Quadrupole Focusing

The traditional method for focusing compact linear amplifiers, such as the TWT, uses an alternating PPM focusing lattice. Motivation for using the PPM focusing scheme over the solenoidal magnet is the decrease in size and weight of the whole focusing system. With a standard permanent magnet, if the magnet length is increased by a factor of N, then all other dimensions of the magnet, i.e., the inner and outer radii, must also be increased by a factor of N to maintain the same magnetic flux inside the magnet. The volume, and also the weight, of the magnet increases to N^3 times its initial value. Using an alternating PPM structure instead increases the weight only by a factor of N for an additional length N, saving a factor of N^2 from the weight of the magnet. The PPM focusing scheme functions well for transporting beams of low to moderate current densities

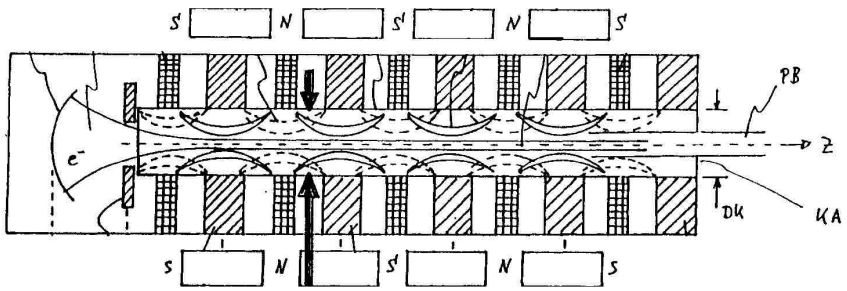

Figure 1.2: Typical PPM focusing lattice featuring a continuously varying field, invented by Mendel, Quate, Youkum [1].

but fails to transport higher current density beams as it cannot produce sufficient magnetic fields for stable transport. A PPM lattice schematic can be seen in Fig. 1.2 where it is clear that the magnetic fields are longitudinal to the direction of beam propagation, and as the periodicity gets smaller the peak fields are significantly reduced by the proximity of the adjacent magnet; this effect is termed field bucking. As will be explored more in Chapter 2, the peak field of the PPM lattice is heavily limited by geometry and as the device dimensions get very small the maximum magnetic field that can be produced is very low. A PMQ lattice is not expected to have the same limitation because the focusing fields are essentially transverse to the beam.

An ideal quadrupole magnet would have four poles with a continuous magnetization vector ($\overrightarrow{M}$) rotation, as in Fig. 1.3. This continuously varying $\overrightarrow{M}$ produces the strongest magnetic field gradients. As can be seen from the figure, the magnetic field on axis inside this ideal quadrupole magnet is a null; however, the quadrupole magnet will produce very strong magnetic field gradients on axis. A permanent magnet in a PPM lattice uses the field on axis to focus and/or transport the electron beam, whereas the quadrupole uses the magnetic field gradient on axis. The Halbach 16-piece model which will be used in this work is a segmented approximation of the ideal quadrupole. The PMQ lattice is built on the FODO principle from optics, where FODO stands for focus-drift-defocus-drift. The FODO principle states that a focusing lens followed by a drift section and then a defocusing lens has a net "strong" focusing. As illustrated in Fig. 1.4, the first element of the FODO

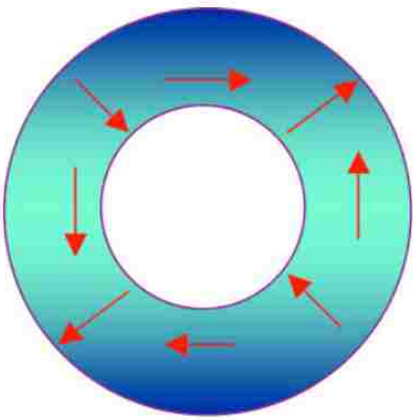

Figure 1.3: An ideal quadrupole magnet.

lattice being employed in the PMQ schematic focuses the electron beam in the x–z plane while defocusing the beam in the y–z plane. The following element in the lattice is rotated 90 degrees and does the opposite, namely, focuses in the y–z plane and defocuses in x–z plane, creating a net focusing effect in both planes. Two quadrupole magnets, or elements, and two drift sections are defined as one lattice period S.

Recent work [2] has demonstrated that quadrupole focusing has the potential to provide strong focusing for space–charge dominated beams. It was also demonstrated that a PMQ lattice focuses an equivalent beam as a PPM using 1/3 the magnetic material. Further, the work suggests that quadrupole focusing lattices can make much larger focusing fields than can be obtained by traditional PPM focusing lattices. These advantages suggested by [2] suggest that the PMQ focusing method could allow us to design new TWT devices for higher frequencies and higher powers.

In addition to the potential to be able to stably transport higher current density beams, a PMQ lattice is much lighter and smaller than the comparable PPM lattices as seen in Fig. 1.5, and Table 1.1 borrowed from [2], where l_q is the magnet width in the z or longitudinal to beam propagation direction, S is the period, and lattice occupancy λ_{occ} is defined as the ratio $\frac{2l_q}{S}$. This size and weight advantage alone is very strong motivation for using the

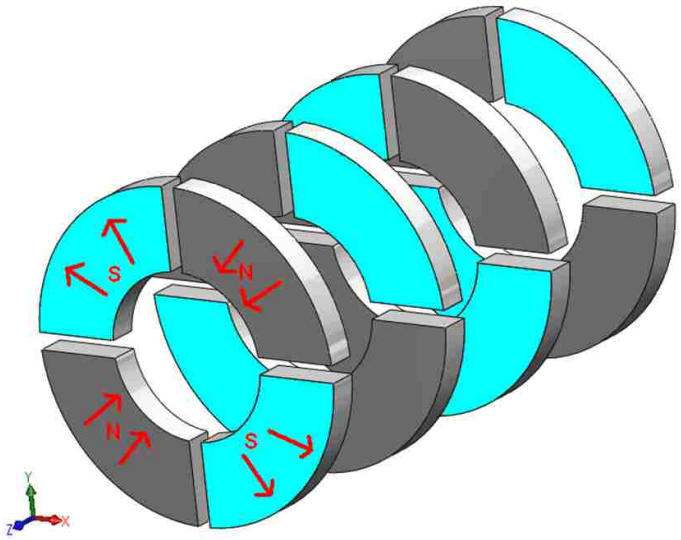

Figure 1.4: The PMQ lattice employing the FODO principle.

PMQ focusing method as it significantly lowers cost and increases portability. Moreover, we believe that PMQ focusing can solve a bigger problem of high frequency devices, and that is the problem of emittance growth. The force due to emittance scales as $1/r^3$, where r is the beam radius; thus, emittance is an important consideration for electron beams with small radii. Recent literature has also emphasized the importance of emittance for this regime [9], [10]. It will be shown through Sherzer's theorem [11] that focusing using multipole magnets can greatly reduce or eliminate emittance growth all together. These are strong advantages for employing PMQ focusing lattices over PPM in these devices.

Table 1.1: Design parameters for PMQ and PPM focusing for comparable beam.

Design Parameter	PMQ	PPM
Magnet length l_q	0.81 mm	3.56 mm
Outer magnet radius r_o	12.0 mm	13.72 mm
Inner magnet radius r_i	4.00 mm	5.05 mm
Lattice Period S	12.46 mm	11.94mm
Lattice occupancy λ_{occ}	13%	59.6%
Magnet volume	326 mm^3	1820 mm^3

Despite these advantages PMQ focusing has many of its own challenges to address.

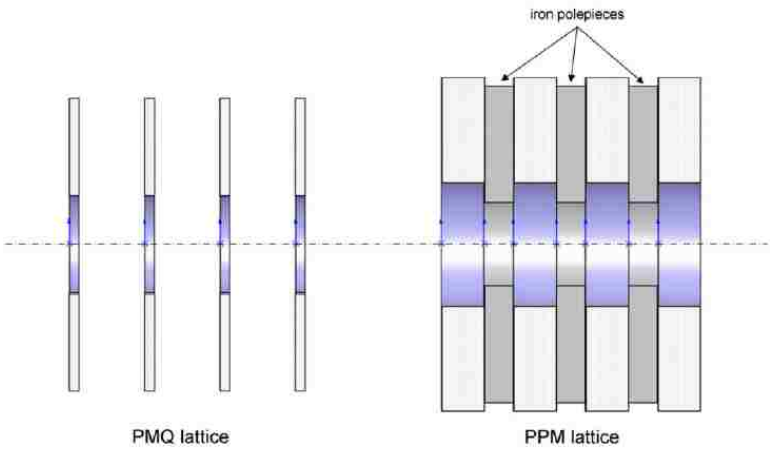

Figure 1.5: Demonstration of the size and weight advantage of PMQ over PPM from [2].

PMQ focusing has never been used for VEDs and, with the exception of [2],[12], the published literature on it is scant. The practical aspect of implementing a PMQ focused electron beam presents many challenges and it will be essential to demonstrate experimentally that beam transport can be achieved using PMQ for space–charge dominated beams. Firstly, a PMQ focusing lattice has two axes of symmetry. Therefore the electron beam has two ripples and more complicated beam motion than for other focusing methods. With an exotic beam profile, it will be essential to avoid interception with the beam pipe or there is risk of melting the beam pipe and the interaction circuit. Secondly, strong and small permanent magnets suffer from minute imperfections that could have a huge impact on the beam; this will have to be carefully surmounted. Thirdly, TWTs have flanges which have to be welded on to the TWT tube around the magnets, and permanent magnets are very heat sensitive. To overcome this, an assembly will need to be designed which can be put over a TWT tube with the flanges already welded on. Another challenge will be designing the magnets around the RF input and output ports. Lastly, it will need to be determined whether the exotic beam profile will properly interact with the interaction circuit to produce more RF than can be achieved with the simpler beam profile of PPM focused tubes.

1.4 Previous Work

1.4.1 Wessel-Berg

Wessel-Berg in 1993 at the IEEE International Electron Devices Meeting presented a paper on the potential of focusing high density electron beams using a quadrupole strong focusing permanent magnet lattice [12]. To him it appeared that the main advantages of quadrupole focusing, as opposed to the traditional PPM focusing method, was a stronger field on axis, in large part due to the transverse nature of the fields which do not require pole pieces. He believed that iron pole pieces in the PPM scheme suffer from demagnetization effects and saturation problems at small dimensions, small permanent magnets in such close vicinity would also suffer from demagnetization effects. Both demagnetization and saturation problems are known to become greater issues when dimensions are minute–at extremely high frequencies.

Wessel-Berg, through a coupled mode formalism approach and using the paraxial approximation, analyzed the motion of the beam-edge electrons by dividing them into two ripples. He delineated the first ripple as the expansion and contraction of the circular beam profile, and the second as the elliptical rotation back and forth of the beam. He determined that the second ripple was dominant and concentrated on that component alone in the lattice design equations. He presented lattice design equations from the dominant ripple driven by the space-charge field and from a second focusing condition from the beam equilibrium condition. In addition to these design equations, he looked carefully at the quadrupole strength using both the maximum possible magnetization and the demagnetization field in the lattice. The latter was calculated numerically using an exact field analysis of the demagnetization field in a four-piece quadrupole. From here he considered two typical examples: the first in the frequency range of 10-20 GHz. He determined that the field needed to focus the beam is very moderate and easily achieved with quadrupole magnets. For the second example he considered the 80-100 GHz range for a millimeter-wave TWT. For this case he also found that the required field strength is easily achievable

using quadrupole permanent magnets. In both cases he kept the beam ripple to 0.2, which is seemingly very reasonable.

His work used the assumption of paraxial theory and he did not perform a full–fledged comparison and evaluation of the two methods. Nevertheless, he verified the basic strong focusing power of a PMQ lattice and the limitation of the field available from PPM focusing, which becomes very small at very high frequencies or at high beam powers.

1.4.2 Work Performed at NRL

In May 2009 in IEEE Transactions on Electron Devices, Abe, Kishek *et al.* published a paper titled, "Periodic Permanent-Magnet Quadrupole Focusing Lattices for Linear Electron-Beam Amplifier Applications." In this paper they describe a lattice design procedure using an envelope code, TRACE3D [13]. More detailed simulations using the electron-gun and beam transport code MICHELLE [14] with magnetic fields from the Ansys code Maxwell [15] and an interaction circuit simulated in WARP [16], of a helical TWT were performed. They developed a PMQ lattice design using the envelope equation for a matched beam under the smooth approximation theory. They used a 16-piece Halbach quadrupole [17]. Using their lattice design, they calculated the size and volume of magnetic material for a comparable PPM lattice and showed that the magnet volume is reduced five-fold. They perform a design for a 16 keV, 0.81 A, 0.33 mm initial radius beam and verified transport using fully 3D PIC simulations.

The nature of the PMQ schematic and the orientation of the forces in the FODO scheme causes an unusual beam profile to form. As the beam travels in the axial direction z through one period, S, it's transverse profile forms an ellipse, longer in x than in y, briefly becomes circular, and then is forms an ellipse with the magnitudes of the axis switched in the x and y directions, before briefly becoming circular again. Although it was beyond the scope of their paper to self-consistently analyze the PMQ focused beam in an interaction circuit, they did examine the interaction of the electromagnetic waves on a helix circuit with round beams of radii corresponding to the minimum and maximum radii

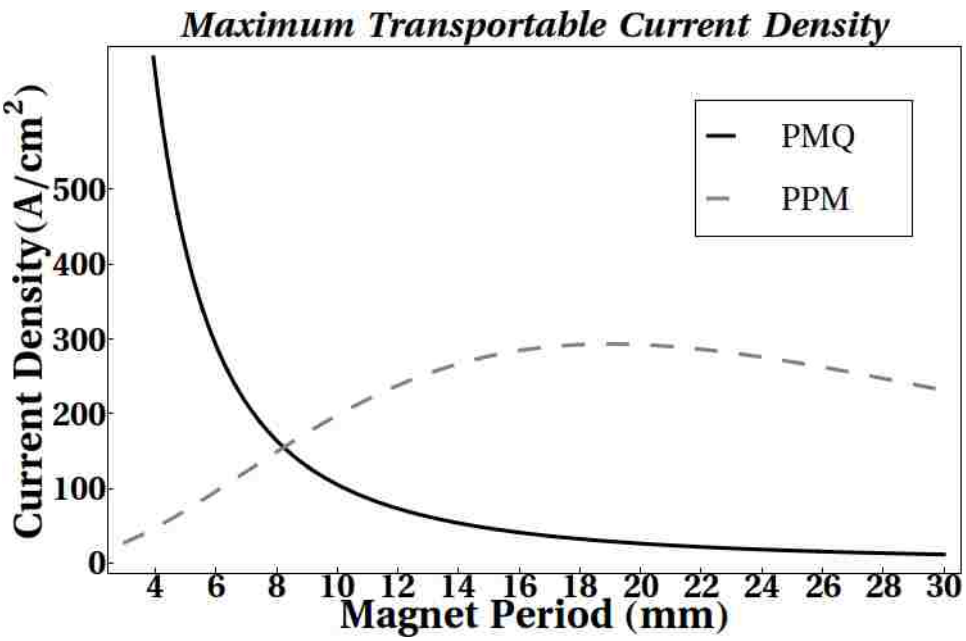

Figure 1.6: Maximum transportable current density per lattice period from Eq. 1.5, and Eq. 1.6 motivated by [2].

of the PMQ beam envelope. These simulations were performed using the 1-D large signal helix TWT code WARP. They explored the sensitivity of the amplifier performance to the two extreme beam radii and determined that, over the radial variation of the elliptical beam, the coupling impedance of the circuit varies approximately 6 percent. This is an excellent result, demonstrating that the electromagnetic beam-wave interaction is relatively insensitive to the radial variation of the elliptical beam. It was determined that the gain per unit length was $\approx$ 5.6 dB/cm and 6.3 dB/cm for the two beam radii, whereas the gain is only 3.3 dB/cm for the PPM focused beam with a PPM focusing lattice of the same periodicity. While they verified the basic methodology and codes, and illustrated the benefits afforded by the strong focusing PMQ lattices, there was much work left to be done.

The NRL work included a comparison of PPM vs. PMQ focusing for maximum transportable current as a function of lattice period. The estimation of maximum transportable current density follows from their equation 6, which is reproduced here as Eq. 1.5.

$$I_{PMQmax} = \frac{(\sigma_0 a_0 \beta\gamma)^2}{4S^2}[\frac{2}{I_A \beta\gamma} + \frac{\epsilon_{n1}^2}{I_1 a_0^2}]^{-1}, \tag{1.5}$$

where a_0 is the mean beam radius, σ_0 is the zero-current phase advance, S is the lattice period, ϵ_{n1} is the normalized emittance for a beam of current I_1, and I_A is the Alfvén current, or approximately 17.1 kA.

The estimate of maximum transportable current for PPM focused beams follows directly the method presented in [2]. It is determined by equating the on-axis magnetic field value estimate to the Brillouin field on axis and solving for maximum current, assuming balanced magnetic and space-charge forces. This is presented as Eq. 1.6 below, where B_r is the magnetic field necessary for Brillouin flow, V_k is the beam voltage, and r_i, r_o are the inner and outer magnet radii, respectively. Note that the current transported using PPM focusing cannot be increased arbitrarily by increasing the lattice period L, but rather, is subject to a stability criterion, which will be explored in more detail later.

$$I_{PPMmax} = \left(\frac{a_o {V_k}^{1/4}}{8.32\text{x}10^{-4}}\right)^2 \frac{B_r^2 S^2 (\gamma\beta)^3}{32} \left(\frac{1}{\sqrt{r_i^2 + \left(\frac{S}{4}\right)^2}} - \frac{1}{\sqrt{r_o^2 + \left(\frac{S}{4}\right)^2}}\right)^2. \tag{1.6}$$

In Fig. 1.6, Fig. 7 from [2] has been recreated, except with current density given in absolute units instead of being normalized. This figure represents a 16 keV beam with an inner magnet radius of 4 mm and indicates a strong advantage for transporting higher current density pencil beams in cases where a shorter lattice period is appropriate. However, Eq. 1.5 depends on the assumption of a hard-edged quadrupole model which, as will be shown, does not apply to quadrupole lattices of relevant dimensions for focusing space-charge dominated beams. A hard-edge model neglects the fringing fields of a magnet and treats the magnetic field as if it were constant over the length of the magnet and zero outside the magnet length, as shown in Fig. 1.7. A PMQ focusing lattice with magnetic

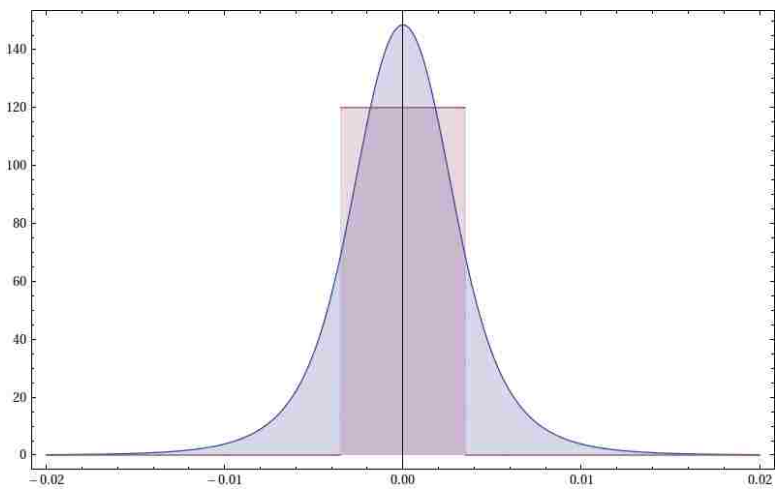

Figure 1.7: Hard-edge magnetic field model, purple, vs. realistic magnetic field model, blue.

fields sufficient to focus a space-charge dominated beam requires the permanent magnet lenses to be placed close together such that the fringing fields from each lens overlap. The effect of the overlapping fields is to significantly reduce the overall field strength compared to the field strengths calculated using the hard-edge quadrupole field model. As such, the hard-edge quadrupole field model is not sufficient for estimating transportable current density for space-charge dominated beams.

The remainder of this dissertation is organized as follows. Chapter 2 will explore the development of the PPM magnet models that is used, both the analytic field profiles and simulations which agree with the analytic models for PPM, as well as analytic analysis of an electron beam traversing this focusing schematic. Chapter 3 will explore the development of the PMQ magnet model, analytically, with simulations, and pertaining to the beam. Chapter 4 covers the development of the envelope codes written to study the physics of the particle beam being transported through the focusing lattices. Chapter 5 studies emittance growth due to the focusing lattices. Chapter 6 discusses PMQ focusing of other beam geometries and other PMQ applications. Chapter 7 summarizes the results and discusses future work.

Chapter 2

PPM Lattices for Electron Beam Transport

In this chapter, we analyze in detail the magnetic fields produced by permanent magnets which will transport the electron beams, specifically for the PPM lattice geometry. The strength of the magnetic field that can be produced will directly correlate to how much current density can be transported in a beam for a given beam energy. It is essential for these purposes to understand the interactions of magnets with their neighboring magnets as this determines the maximum magnetic field that can be produced on axis. PPM lattices are presently the transport method of choice for most compact linear vacuum RF sources. It is essential to understand the limitation of PPM transport in relation to PMQ transport in the following chapter.

2.1 PPM Magnet Model

Solenoidal magnetic fields generated by permanent magnets, especially when iron pole pieces are used and when multiple solenoidal magnets are nearby each other, are not trivial to understand. However, if we can determine the field on axis, we can expand the field

off-axis using only the derivatives on axis for axisymmetric geometries. The lowest order expansion of the field off-axis is known as the paraxial approximation and is commonly used for beam physics calculations. The on-axis field for a loop of current is obtained using the Biot-Savart Law:

$$B_z = \frac{\mu_0}{2}\frac{Ia^2}{(a^2+z^2)^{3/2}}, \tag{2.1}$$

where μ_0 is the permeability of free-space, a is the radius of the current loop, z is the distance from the center of the loop to the observation point, and I is the current carried by the loop. To obtain the field from a finite solenoid, we need to integrate this loop for $z_1 \leq z \leq z_2$ and $r_i \leq a \leq r_o$, where z_2 - z_1 is the length of the solenoid and r_i, r_o are the inner and outer radii of the solenoid, respectively. The axial integration for n turns per unit axial length and a radial current differential of $\frac{dI}{dr}$ gives:

$$dB_z = \frac{\mu_0 n}{2}\frac{dI}{dr}\left(\frac{z-z_1}{\sqrt{(z-z_1)^2+r^2}} - \frac{z-z_2}{\sqrt{(z-z_2)^2+r^2}}\right). \tag{2.2}$$

After the radial integration, we have:

$$B_z = \frac{\mu_0 nI}{2(r_o-r_i)}\left((z-z_1)\xi - (z-z_2)\xi\right), \tag{2.3}$$

where

$$\xi = \log\frac{\sqrt{(z-z_1)^2+r_0^2}+r_0}{\sqrt{(z-z_1)^2+r_i^2}+r_i}. \tag{2.4}$$

Equation 2.3 can now be used to find the fields everywhere due to a finite solenoid using the on-axis expansions. To convert this from a solenoidal field to the field from a finite cylindrical permanent magnet, also known as a pillbox magnet, we need to look at the magnetic moments of permanent magnets.

In general, the magnetic flux density is given by

$$\vec{B} = \mu_0\left(\vec{H}+\vec{M}\right), \tag{2.5}$$

where $\mu = \mu_0(1 + \chi_m)$, χ_m is called the magnetic susceptibility and is dimensionless. A permanent magnet has a total magnetic dipole of $\vec{m} = \vec{M}V$ where $\vec{M}$ is the magnetic moment, and V is the volume of the cylinder. The magnetic remanence field is the magnetic flux density when $\vec{H} = 0$; this field is called B_r. We can represent axisymmetric permanent magnets using surface currents in a similar way to solenoids. The magnetization $\vec{M}$ results from an internal distribution of magnetic moments $\vec{m}$ such that a volume element dv has a magnetic moment of $d\vec{m} = \vec{M}dv$. These magnetic moments are equivalent to a current flow and each moment $d\vec{m}$ produces a current density of the form $\vec{J} = \frac{d\vec{m}}{dS}$. Using Ampere's Law, the vector potential due to $d\vec{M}$ is

$$d\vec{A}(\vec{r}) = \frac{\mu_0}{4\pi}\frac{d\vec{m} \times \vec{r}}{|\vec{r}|^3}. \tag{2.6}$$

The total vector potential A for a summation of all magnetic moments in a given volume is found by integrating the above expression:

$$\vec{A}(\vec{r}) = \int_V \frac{\vec{\nabla} \times \vec{M}}{r} dV + \int_S \frac{\vec{M} \times d\hat{n}}{r} dS. \tag{2.7}$$

We can take the surface outside of the magnet. Doing so eliminates the second integral, and the first integral implies a magnetic current of the form

$$\vec{\nabla} \times \vec{M} = \vec{J_m}. \tag{2.8}$$

For a uniform magnetization, as in a permanent magnet, the fields produced by the magnetization can be equivalently represented by surface currents on the volume.

We are now justified in replacing the magnetic flux density from the ideal solenoid $\mu_0 n\frac{dI}{dr}$ with the remanence field from the permanent magnet, B_r, in Eq. 2.3 and have a model for the on-axis magnetic field due to an annular permanent magnet:

$$B_{z,r=0} = \frac{B_r}{2}\left(\frac{z - z_1}{\sqrt{(z - z_1)^2 + r_{edge}^2}} - \frac{z - z_2}{\sqrt{(z - z_2)^2 + r_{edge}^2}}\right) \tag{2.9}$$

where the magnet extends from z_1 to z_2 and r_{edge} is the radius of the outside of the magnet. By alternating the direction of this field and using superposition, a full model of

the magnetic field from a PPM lattice is achieved as

$$B_{PPM} = \sum_{i,n=2} \frac{B_r}{2}(inner - outer) + \sum_{i+1,n=2} \frac{B_r}{2}(-inner + outer) \tag{2.10}$$

where

$$inner = \left(\frac{z + z_1 - Si}{((z + z_1)^2 + r_i^2)^{1/2}} - \frac{z + z_2 - Si}{((z + z_2)^2 + r_i^2)^{1/2}} \right), \tag{2.11}$$

and

$$outer = \left(\frac{z + z_1 - Si}{((z + z_1)^2 + r_o^2)^{1/2}} - \frac{z + z_2 - Si}{((z + z_2)^2 + r_o^2)^{1/2}} \right), \tag{2.12}$$

S is the period, the summation is over index i, and n is the index step. This model will be used to understand multi-magnet interactions to get a better understanding of the PPM model and its limitations. In Chapter 4 this model of the fields will be implemented in the PPM envelope code.

A comparison of a "pillbox" magnet, i.e. a magnet whose inner radius is finite with no outer radius, and a finite permanent magnet as used for PPM focusing is evident in Fig. 2.1 and shows the complicated field profiles achieved with permanent magnets. The peak fields of the pillbox magnet are very close to the remanence field of 1.2 Tesla of a neodymium permanent magnet until the magnet becomes very short. The fields from the finite magnets, however, are significantly more complicated, with much lower central fields and large field magnitudes at the ends for longer magnet lengths.

2.1.1 PPM Multi-Magnet Interactions

A detailed analysis of the PPM fields as they relate to beam dynamics will be given in the next section where we will assume a sinusoidal field profile. Here we analyze the fields with the permanent magnet model we established in the previous section. Note that this model does not account for the iron pole pieces that are used in practice to strengthen and smooth the fields.

First, Figs. 2.2, 2.3, and 2.4 show the PPM field from stacks of magnets with 1.25 cm, 2.5 cm, and 5 cm lengths, respectively. All figures are for inner magnet radii of 1.25

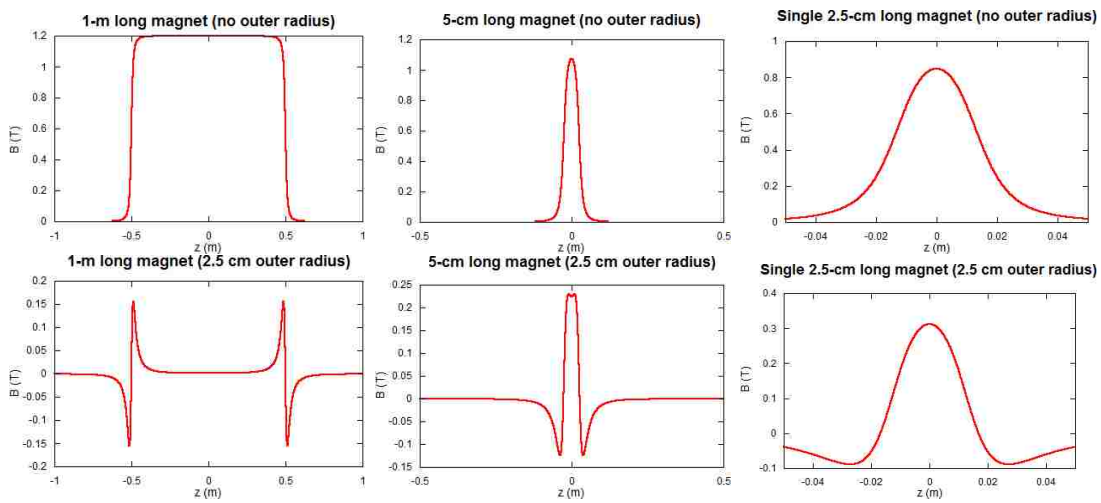

Figure 2.1: Effects of finite radius in permanent magnets.

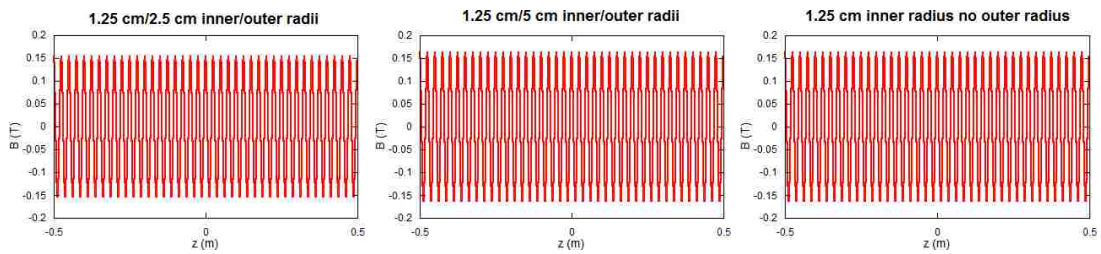

Figure 2.2: B-field profiles for l_p= 1.25 cm.

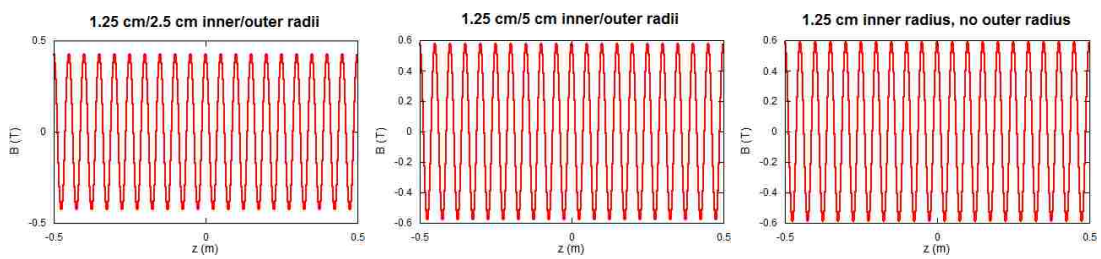

Figure 2.3: B-field profiles for l_p= 2.5 cm.

cm, and include outer magnet radii of 2.5 cm, 5 cm, and infinite size. We summarize the peak magnetic field in Table 2.1, along with the cases for 10-cm and 20-cm long permanent magnets.

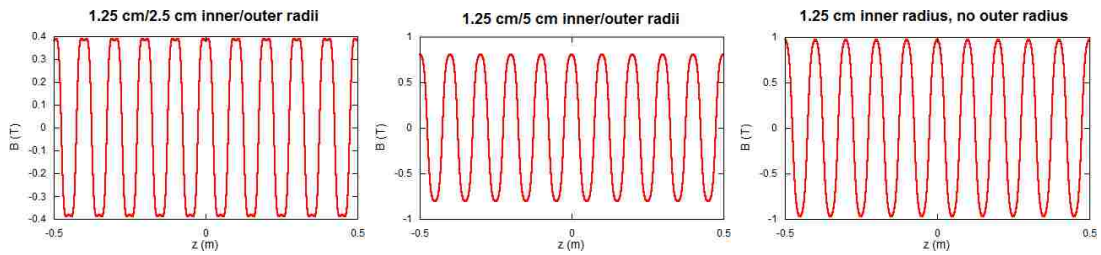

Figure 2.4: B-field profiles for l_p= 5.0 cm.

Table 2.1: Peak field strengths - r_i = 1.25 cm, various outer radii.

Magnet Length l_p	r_o = 2.5cm	r_o = 5cm	r_o = infinite
1.25 cm	0.153 T	0.163 T	0.163 T
2.50 cm	0.426 T	0.579 T	0.589 T
5.00 cm	0.388 T	0.809 T	0.971 T
10.0 cm	0.323 T	0.644 T	1.13 T
20.0 cm	0.313 T	0.591 T	1.18 T

It is clear that as the pillbox magnet length, l_p, increases, the outer magnet radius needs to increase to achieve the asymptotic field. The asymptotic field is defined as the peak field obtained with an infinite outer radius. However, as the magnet length decreases, the asymptotic field is achieved with significantly decreased outer magnet radii. For us this means that when using thin magnets, the outer magnet radius does not need to be large. What we also observe, given that the magnet period in Fig. 2.2 is one quarter the period as that in Fig. 2.4, is that the asymptotic field is significantly reduced by using shorter magnet periods, in this case by 85%. This reduction in asymptotic field can be attributed to the zero crossing of the field between magnets whose fields are in opposite directions. This is field bucking, as was defined earlier. This is the effect of multi-magnet interactions, and is very significant for small lattice periods.

One can also observe that, for small lattice periods, the magnetic field can be easily estimated by a sine function, but when the magnet length becomes longer, as in Fig. 2.5, the field pattern becomes highly non–sinusoidal. In the analysis in the next section, we will assume a sinusoidal pattern and assume shorter magnets, less than 2.5 cm.

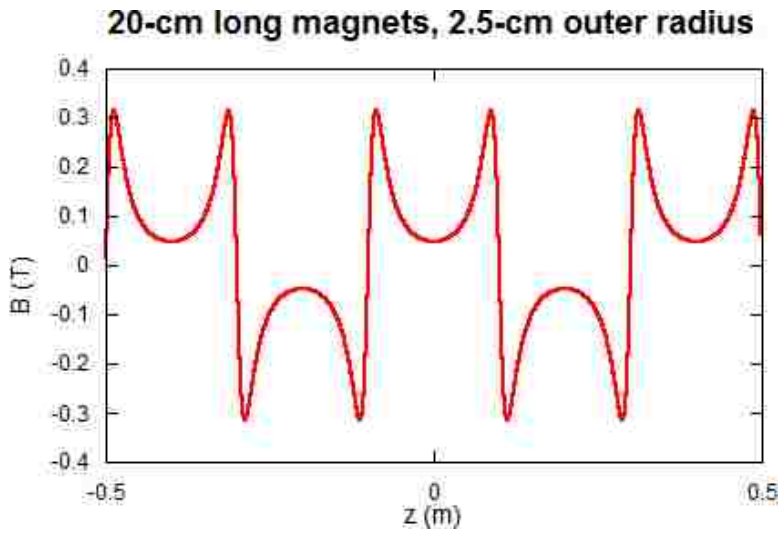

Figure 2.5: Highly non–sinusoidal PPM field with long magnet period.

From the multi-magnet interactions, it is obvious that there is an on–axis field drop–off with decreasing period S. This field drop–off is plotted in Fig. 2.6, as a function of the inner magnet radius, and will be a key part of the maximum transportable current for PPM lattices.

2.2 PPM Limitations

Periodic focusing is separated into two main classes, thin lens focusing, and continuously varying fields. The main difference between the two is the separation of the focusing lenses. In order to transport lower-energy (space-charge dominated) electron beams, it is necessary to use continuously varying fields. Higher energy electron beams, which are termed "stiff" because of their velocities, are emittance-dominated beams and can be successfully transported using thin–lens focusing. For beam transport in TWTs, the two common transport methods are solenoids and PPM focusing. The motivation for using PPM focusing is a reduction in weight compared to a solenoid and no power supplies or external cooling required, making PPM focusing systems much more compact and lightweight than solenoids.

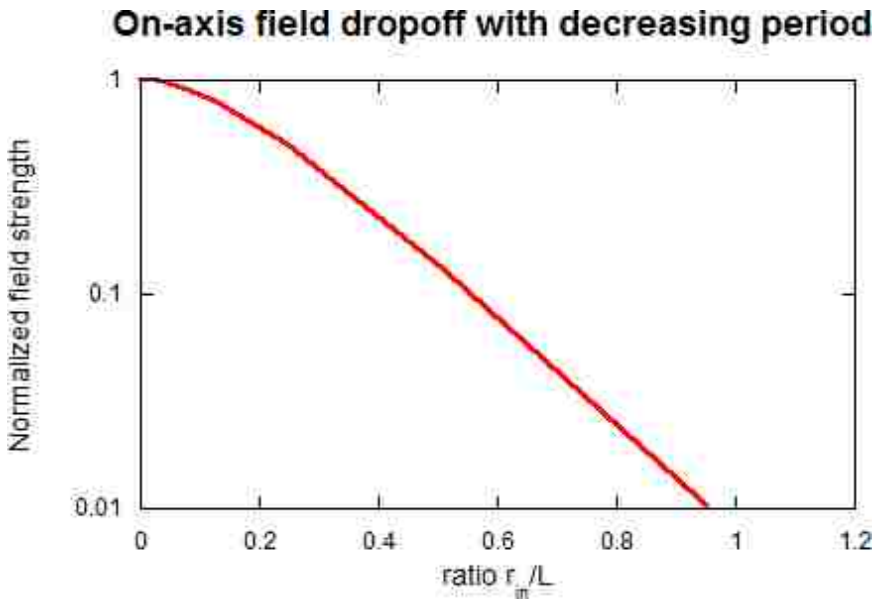

Figure 2.6: PPM field dropoff for decreasing period S, infinite outer radius.

PPMs, however, can only transport Brillouin flow, as opposed to the confined flow that solenoids can transport. The basic PPM schematic was introduced in Chapter 1, and as can be seen from Fig. 1.2, and also from Fig. 2.4 the magnetic field will be continuously varying. We can assume the form for the axial magnetic field to be sinusoidal and estimate it by:

$$B_z(z) = B_p \cos \frac{2\pi z}{S}, \tag{2.13}$$

where B_p will be the maximum magnetic field, and L is the period of the focusing lattice. Using conservation of canonical angular momentum, also known as Busch's Theorem, and keeping lowest order terms approximation, we can solve for the azimuthal velocity component as:

$$\dot{\theta}[z] = \frac{e}{2m\gamma}\left(B_p \cos\left(\frac{2\pi z}{S}\right) - \frac{r_c^2}{r^2}B_c\right), \tag{2.14}$$

where B_c is the magnetic field on the cathode, and r_c is the beam radius at the cathode. Substituting in for the azimuthal velocity solved in Eq. 2.14, the radial equation of motion becomes:

$$r'' = \frac{I}{I_A}\frac{2r}{\beta^3\gamma^3 r_b^3}\left(1 - \frac{B_p^2}{B_{BR}^2}\frac{1+\cos\left(\frac{4\pi z}{S}\right)}{2}\right), \tag{2.15}$$

where B_{BR} is defined below. This is a key PPM design equation. Mendel et. al [1] showed that a minimum beam ripple is achieved if $B_p = \sqrt{2}B_{BR}$. Equation 2.15 can be rewritten as what is called the Universal PPM Equation:

$$\frac{d^2\sigma}{dT^2} + \alpha[1-\cos(2T)]\sigma - \beta_{SC}\sigma = 0 \tag{2.16}$$

where $\sigma = r/a$, $T = \frac{2\pi z}{L}$, $\alpha = \frac{S^2}{4\pi^2}\frac{I}{I_A}\frac{B_p^2}{\beta^3\gamma^3 r_b^2 B_B R^2}$, and $\beta_{SC} = 2\frac{S^2}{4\pi^2 r_b^2}\frac{I}{I_A\beta^3\gamma^3}$. This universal equation describes the beam trajectory in terms of the normalized beam edge radius σ, and the normalized axial distance T. It is used commonly in PPM design [18]. If σ'' is small, the cos term in Eq. 2.16 can be neglected and the equation is reduced to

$$\frac{d^2\sigma}{dT^2} + \alpha\sigma - \beta_{SC}\sigma = 0. \tag{2.17}$$

where α is the magnetic field coefficient, and β_{SC} is the space–charge coefficient. The flow is considered balanced if $\alpha = \beta_{SCC}$, which is equivalent to $B_p^2 = 2B_{BR}^2$, where B_{BR} is the magnetic field necessary for Brillouin flow. When $\alpha \neq \beta_{SC}$ and there is either insufficient magnetic field or excess magnetic field there will be larger oscillations than the design ripple [19].

Equation 2.17 is an equation of the Mathieu type, and follows the well known Mathieu stability condition which has stability pass and stop bands on the scale of parameter α. The pass bands are located at

$$\alpha < 0.66, 1.72 < \alpha < 3.76, \text{ and } a > 6.10, \tag{2.18}$$

where α is a parameter that quantifies the amount of "ripple" or radial variation in the beam edge. To maintain a low ripple, the maximum practical α is about 0.2. Using this parameter and the fact that PPM structures can only transport Brillouin flow beams, we

can calculate the maximum transportable current density as a function of lattice period S. To do this we set the magnetic field required for Brillouin flow equal to the magnetic field from the PPM lattice from the focusing parameter α and solve for the current density. The Brillouin field is

$$B_{BR}^2 = \frac{\sqrt{2}I_0}{\pi\epsilon_0|\eta|V_0^{1/2}a^2(\gamma\beta)^3}. \tag{2.19}$$

Then solving for I and converting it to current density J, the maximum current density that can be transported in a PPM stack is given by

$$J_{PPM} = \pi r_b^2 \alpha I_A (\gamma\beta)^3 \frac{2\pi^2}{S^2}, \tag{2.20}$$

requiring a peak field strength of

$$B_r = 4\pi \frac{mc\gamma\beta}{eS}. \tag{2.21}$$

It seems easy enough to be able to transport arbitrarily high current densities by just deceasing the period S. However, decreasing S will tend to reduce the possible field on–axis, as we saw from the field drop–off in Fig. 2.6. Equation 2.20 was plotted in Chapter 1 as Fig. 1.6

In practice, PPM lattices employ iron pole pieces between and around the PPM magnets. The effect of the pole pieces is to limit the external magnetic field, smooth the field profile between magnets, and amplify the center field somewhat. Pole pieces do effectively increase the maximum current density transportable. We use the field models without pole pieces because the analytic expressions are much more straight forward and demonstrate the same magnet effects. PPM design criteria, including pole pieces, can be found in [20]. Pole pieces do suffer from some limiting effects in high-frequency tubes, namely, they can suffer from saturation and demagnetization effects which are amplified at small dimensions. The PPM field model developed here in this chapter will be used in the envelope codes developed in Chapter 4 to analyze the beam dynamics for various parameters as well as look at the maximum transportable current density for PPM which can be compared exactly to the same parameters for PMQ focusing lattices.

Chapter 3

PMQ Lattices for Electron Beam Transport

In this chapter we begin by discussing how the analytic model for the fields from quadrupole magnets were created and verified. Simulations are presented to verify the analytic model and for use with subsequent simulations. Subsequently, the quadrupoles' ability to produce high fields on axis will be analyzed with respect to the multi-magnet interactions. An equation is presented for calculating the field drop–off observed with multi-magnet interactions. Lastly, analytic beam transport equations for PMQ lattices are analyzed with respect to the amount of current density that can be transported using this method.

3.1 PMQ Analytic Magnet Model

Following the choice of the NRL team to use a segmented 16-piece Halbach quadrupole permanent magnet in their designs, we developed an analytic model for the fields to use in our envelope code. The 16-piece Halbach magnet is chosen over the traditional 4–piece quadrupole magnet model as it can achieve higher magnetic field gradients and approxi-

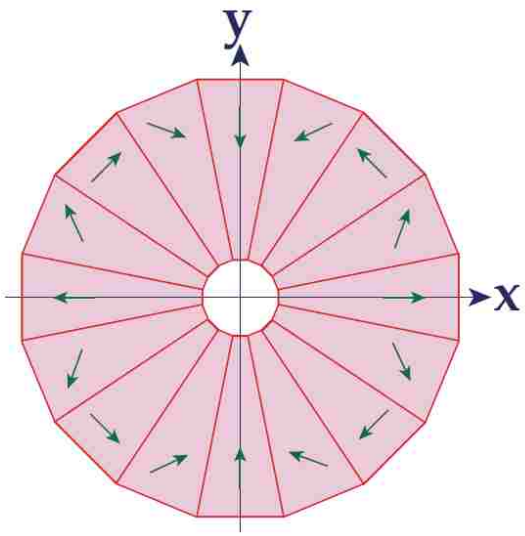

Figure 3.1: Magnetization vectors for the 16-piece Halbach quadrupole magnet [3].

mates the ideal quadrupole presented in Chapter 1.

A PMQ design for a space-charge dominated beam necessarily has magnets which are very close together. The close magnet proximity invalidates the hard-edge approximation which is traditionally used for quadrupole fields in beam-envelope codes such as TRACE3D. It is, therefore, necessary to develop a magnetic field model that accounts for the overlapping fringe-fields from the individual permanent quadrupole magnets. Halbach derived an expression for the fringing magnetic fields for the 16–piece semi–infinite quadrupole magnet [3]. The 16–piece Halbach quadrupole (see Fig. 3.1 for the orientation of the magnetization vectors $\vec{M}$) is chosen to have a 4–fold increase in the gradient of the magnetic field on axis than the standard 4–piece quadrupole magnet [21]. We modify Halbach's expression by subtracting another semi–infinite magnet to represent the fields of a finite width magnet. Then, using the principle of superposition, an analytic expression is developed for the gradient of the magnetic field for a lattice of $n+1$ quadrupole magnets [22], given as

$$\frac{dB}{dx} = \sum_{i=1}^{n} G\mathcal{F}[i, S, l_q] - \sum_{i=2}^{n+1} G\mathcal{F}[i, S, l_q], \tag{3.1}$$

where

$$\mathcal{F} = F\left[-i\left(\frac{S}{2} - l_q\right) + S - \frac{l_q}{2}\right] - F\left[-i\left(\frac{S}{2} - l_q\right) + S + \frac{l_q}{2}\right], \tag{3.2}$$

$$F = \frac{1}{2} - \frac{z}{16}\left(\frac{1}{r_i} + \frac{1}{r_o}\right)\left(\frac{{v_i}^2 {v_o}^2}{v_i + v_o}\left({v_i}^2 + {v_o}^2 + 4 + 8 v_i v_o\right)\right), \tag{3.3}$$

and

$$v_{i,o} = \frac{1}{\sqrt{1 + \left(\frac{z}{r_{i,o}}\right)^2}}. \tag{3.4}$$

The constant G is defined by

$$G = 2B_{pole}\left(\frac{1}{r_i} - \frac{1}{r_o}\right)\mathrm{sinc}\left(\frac{3\pi}{M}\right), \tag{3.5}$$

where M is the number of sections in the quadrupole and B_{pole} is the magnetic flux density at the magnet pole.

The gradient of the magnetic field in the x–z plane is shown in Fig. 3.2 for 9.5 magnet periods, or 19 quadrupoles. The quadrupole lattice geometry and representative symbols are shown in Fig. 3.3, where F represents a focusing lens, and D a defocusing lens.

3.2 Simulated Magnet Model

For verification of this analytic expression, a geometric magnet model was constructed using the Ansoft code Maxwell [15]. The Maxwell model accounts for the complicated

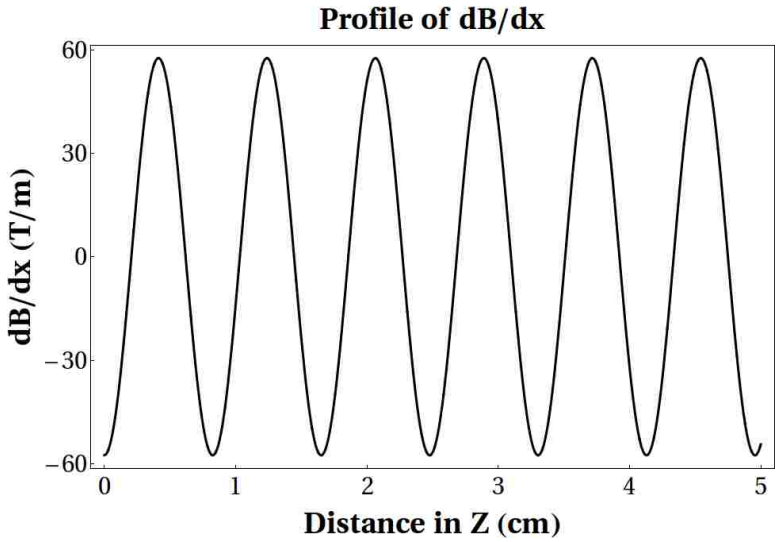

Figure 3.2: PMQ field profile from [3.1].

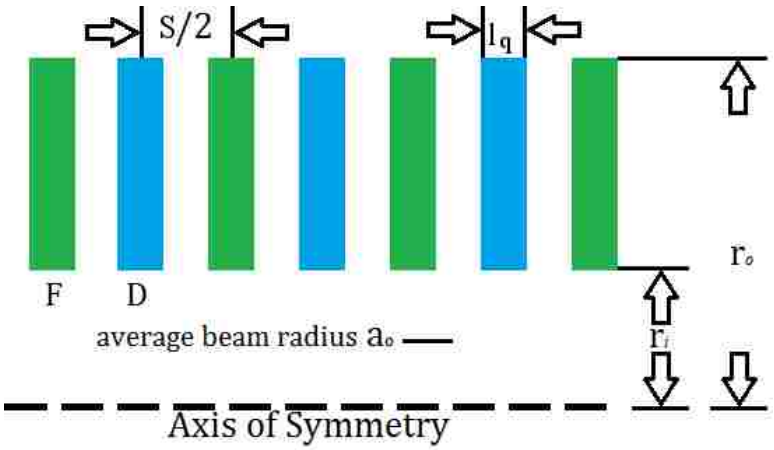

Figure 3.3: Quadrupole lattice geometry.

physics of the permanent magnet interactions. The magnetic material was chosen as $SmCo_{28}$, and the magnetic pole field or residual magnetic field was calculated as 1.2 T.

To compare the simulation results with the results from our analytic model, the exported fields were analyzed using a Python script. To determine the value of the gradient of the magnitude of the magnetic field and to verify its symmetry, the field results were

analyzed with the following definitions of the field gradient. We define the gradient of the magnetic flux density B along the z axis on the positive x axis as:

$$\nabla B_{x^+} = \frac{|B(x=5)| - |B(x=0)|}{\Delta x} \tag{3.6}$$

at each value of $z = -40$ mm to $z = 40$ mm, with $\Delta x = 5$ mm. The gradient of B along the z axis on the negative x axis is given as

$$\nabla B_{x^-} = \frac{|B(x=-5)| - |B(x=0)|}{\Delta x} \tag{3.7}$$

at each value of $z = -40$ mm to $z = 40$ mm, with $\Delta x = 5$ mm. This was performed similarly for positive and negative y. This gives us four versions of the gradient of the magnetic flux density $\vec{B}$ which should be identical if the symmetry that we expect exists in the simulations.

The magnetization vectors were determined by rotating $\vec{M}$ 45° per section with respect to the magnet, each magnet is rotated by 22.5°. Therefore, each magnetization vector is rotated 67.5° with respect to the origin. Note that in determining the orientations of each $\vec{M}$ the approximation $\tan(67.5) \approx 2.41$ was used. Some unexpected anomalies appeared at the peak of the field gradient, as seen in Fig. 3.4. A second tangent approximation with more significant digits was also simulated, the second tangent approximation $\tan(67.5) \approx 2.41421$. It is important for us to understand what level of precision is necessary for the orientation of $\vec{M}$ because the precision with which real magnets will be magnetized should not make a large difference in the resulting focusing fields. If too high precision is necessary the application of this method will not be practical. The gradient using the first tangent approximation to determine the vector positions of each $\vec{M}$ is seen in Fig. 3.4, whereas the second approximation is seen in Fig. 3.5. No appreciable change is noted in the magnitude of the field, or in the anomalies at the top of the graph. The second tangent approximation did slightly improve the symmetry of the simulation, but not the anomalies.

The anomalies seen in Figs. 3.4, 3.5 became worse for wider magnets, and decreased for narrower magnets. Progress was only made on resolving the anomalies by lowering the percentage of acceptable error. By default, simulations were set to a maximum error of

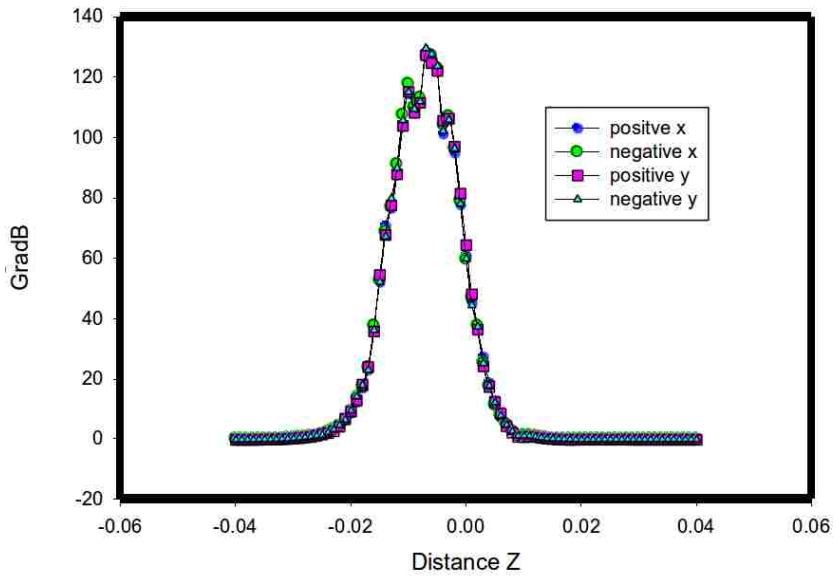

Figure 3.4: Gradient of magnetic flux analyzed using python script for first tangent approximation.

1%. When the error was set to 0.1% the simulation run time was greatly extended, but the anomalies given by the simulation were different. We graph the gradient of B for a magnet with width of 25 mm for the two different error conditions in Fig. 3.6. It would be useful to lower the error even further to improve simulation fidelity, but lowering the error any more than 0.1% demanded more than the 8 GB of computer memory available.

The magnet dimensions used in the simulations for the results that follow were r_i = 7 mm and r_o = 14 mm, while the width of the magnet in the z direction, l_q, is variable. The vector plots from a single quadrupole magnet are shown in Figs. 3.7, 3.8. Note the field symmetry and the transverse nature of the fields interior to the magnets: nearly all the interior fields are in the x–y plane. We can see from these vector plots that the fringing fields are not insignificant. Note that these vector plots physically represent only field magnitude.

To verify that this model is giving us the same field profile as the analytic model, it is necessary to look at plots of the gradient of the magnetic field from our simulations and

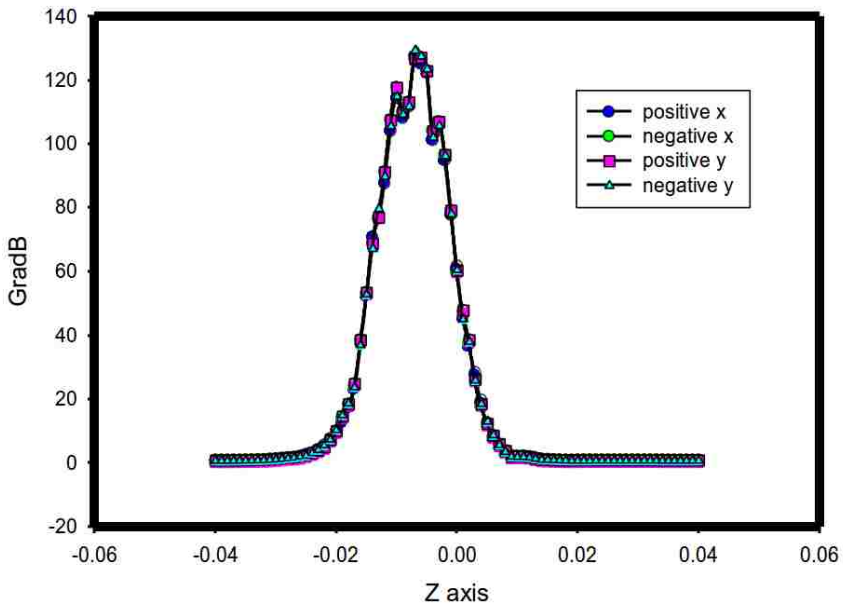

Figure 3.5: Gradient of magnetic flux analyzed using python script for second tangent approximation.

compare them to the analytic plots. Magnetic field gradient plots are not available directly from the Maxwell code; therefore, the magnitude of the magnetic field was exported onto a grid for points interior to the magnets, with the export grid defined in Table 3.1.

Table 3.1: Export grid for fields (mm).

Axis	min	max	stepsize
x	-5	+5	0.1
y	-5	+5	0.1
z	-40	40	0.5

The magnetic field gradient ∇B_{x^+} is visualized in Fig. 3.9 by looking at the field magnitude on various boxes inside a single quadrupole magnet. The gradient was measured at 45° intervals around the z axis to ensure symmetry, and was found to be consistent. The percent error convergence in the simulations was reduced until the gradients were identical for different error requirements.

The simulations agreed with the analytic calculations within 7% for a variety of mag-

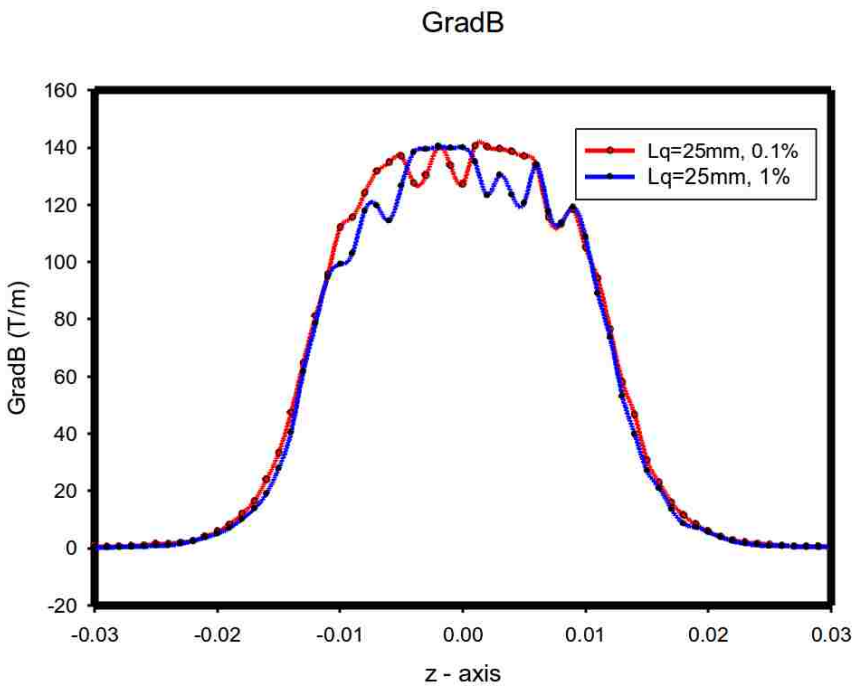

Figure 3.6: Gradient of magnetic flux for magnet width 25 mm with errors of 1% and 0.1%.

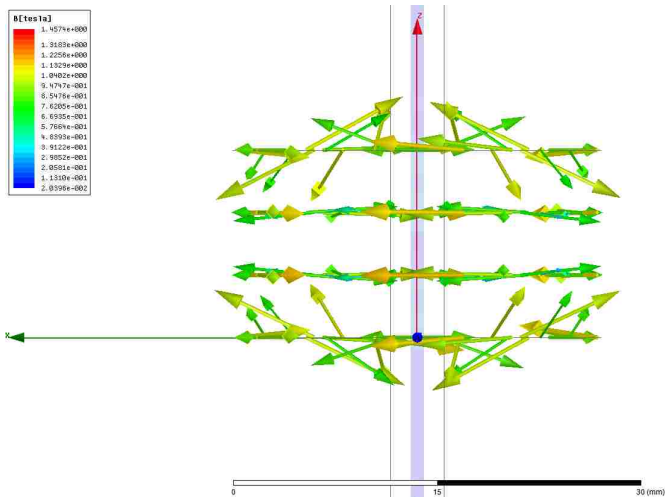

Figure 3.7: B-vectors in the y–z plane showing that most of the field is transverse.

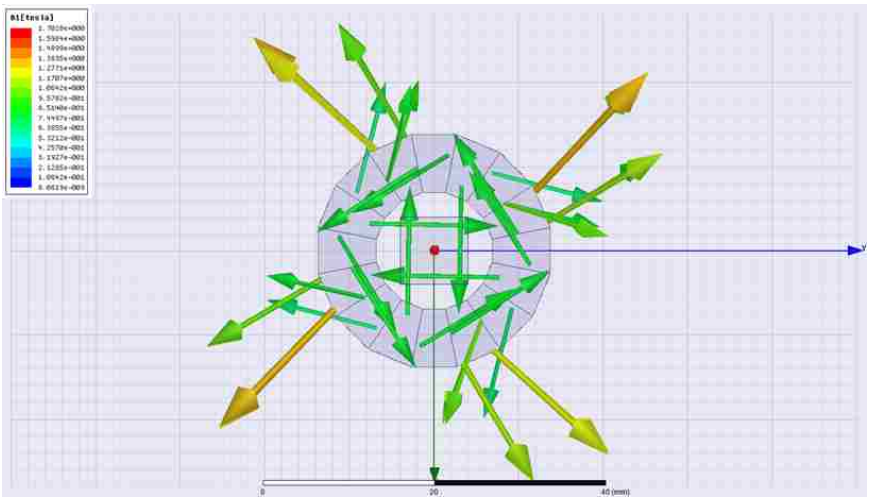

Figure 3.8: B-vectors in the x–y plane.

net dimensions. On average, the simulations gave a field $\approx 5\%$ higher than the analytic model. Therefore, the analytic model was found to be sufficient for the magnet model to be employed in the envelope codes of Chapter 4. A comparison of the analytic model to the Maxwell model for various magnet widths l is shown in Fig. 3.10. This agreement was considered to be excellent.

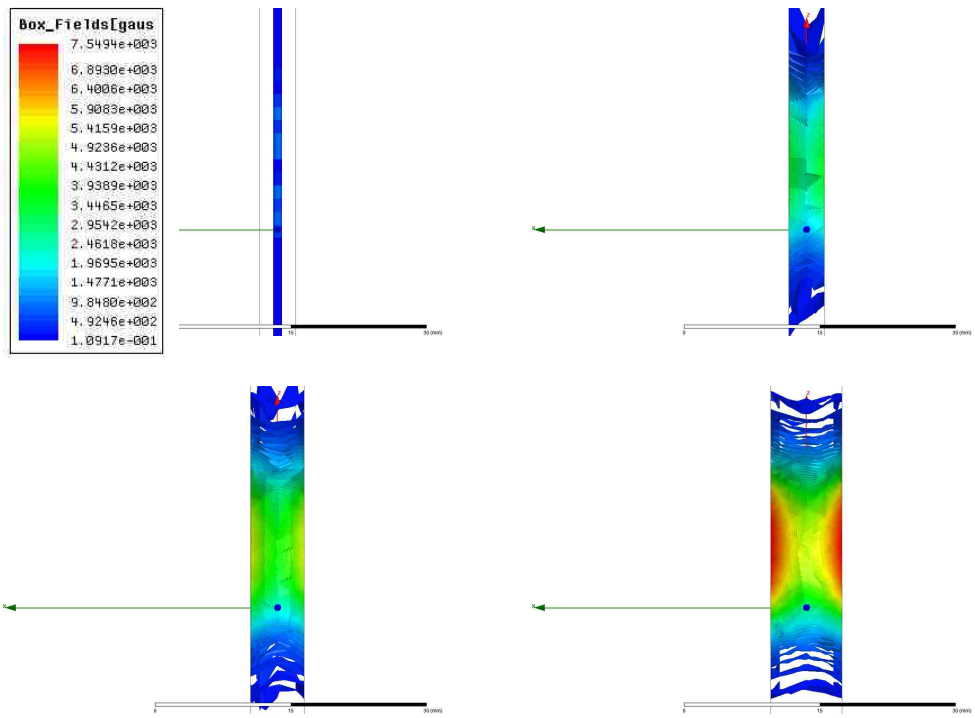

Figure 3.9: Magnetic field inside quadrupole in the y–z plane.

3.3 PMQ Multi-Magnet Interactions

As discussed in Chapter 2 with the PPM magnets, permanent magnets have complicated fields and field interactions that change drastically with magnet dimensions. The multi-magnet interactions for PMQs are equally as important as those for the PPM magnets studied in Chapter 2. In particular, all the work that has been done on PMQ lattices for RF amplifiers has neglected the multi-magnet interactions of the PMQ lattices. The fringing fields of the magnets have a strong interaction which decreases the peak B strength as well as the B_{rms} field strength.

To analyze these interactions, a PMQ magnet model was created using Halbachs' fringe-field model and simulations were performed for a variety of lattice parameters.

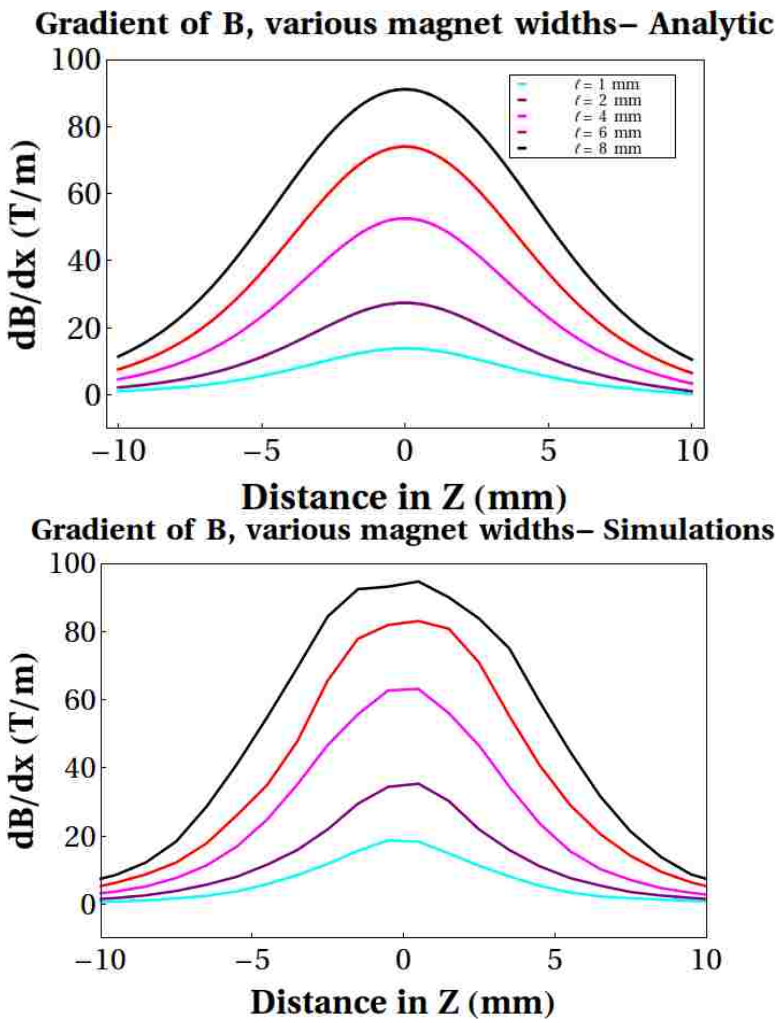

Figure 3.10: Analytic quadrupole model (top) and simulated quadrupole model (bottom). The different colors represent different magnet widths, l, as indicated in the legend.

3.3.1 PMQ - Multi-Magnet Interactions

Multi-magnet interactions for PMQ lattices were studied using the analytic PMQ field model developed in section 3.1. Single magnet simulations were compared to the analytic field model in the previous section, and here we verify that the simulations match the analytic field model for multiple magnets. For this purpose, we simulated two magnet

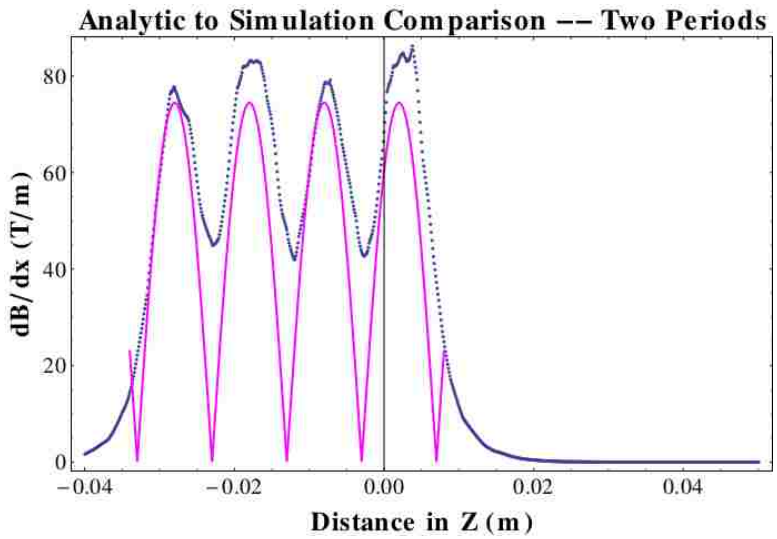

Figure 3.11: Magnetic flux density B for two PMQ periods from simulated quadrupole model (right) and the absolute value of ∇B_x for simulations versus that obtained by Eg. 3.2 (left).

periods in Maxwell and analyzed a two-period set of magnets using Eq. 3.1 and graphed the absolute value of the gradients from both in Fig. 3.11. The magnetic field interior to the magnets for two periods from Maxwell is seen in Fig. 3.12.

We were able to verify that superposition, used to add the linear fields from the analytic model, is sufficient to construct the magnetic field due to a magnet lattice with accurate representation of the multi–magnet interactions.

We performed a parameter scan for various magnet lengths and various magnet periodicities to determine how the peak and rms B fields change with the multi-magnet interactions. In Fig. 3.13 a magnet length of $l_q = 1$ was simulated in a lattice with periodicities: $S = 10$ mm + $\mathrm{l_q}$, 5 mm + $\mathrm{l_q}$, 2.5 + $\mathrm{l_q}$ mm, and $\mathrm{l_q}$. Figure 3.14, and Fig. 3.15 use $l_q = 5$ mm, and $l_q = 10$ mm, respectively, with the same periodicity as defined for Fig. 3.13.

In Fig. 3.13, where a short magnet of length $l_q = 1$ mm (L_q in the figures) is used, the decrease of peak field strength is very dramatic, decreasing from a peak field of 15 T/m

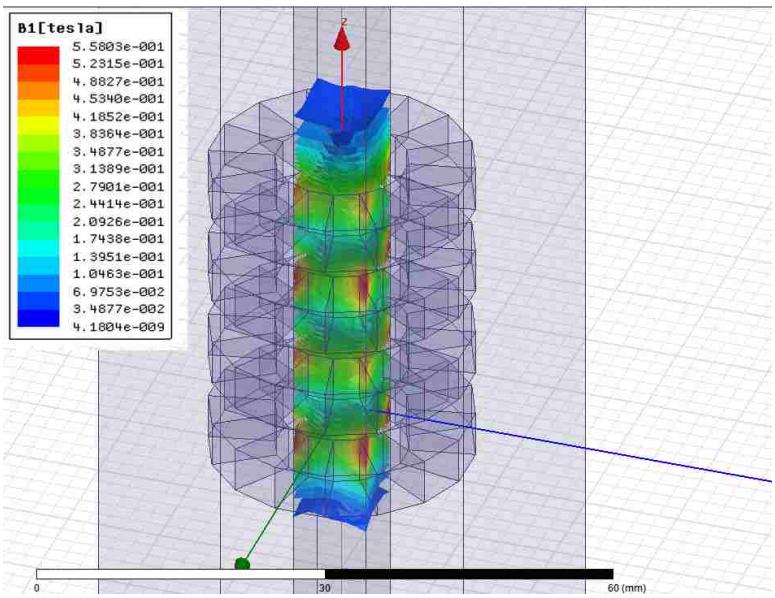

Figure 3.12: Magnetic flux density B for two PMQ periods from simulated quadrupole model.

to a peak field of just 1.5 T/m when the periodicity is reduced from $S = 22$ mm to $S = 7$ mm. The field profile changes completely when these short magnets are placed right next to each other, i.e. the period S is equal to the magnet length $2l_q$. For a slightly longer magnet, as in Fig. 3.14, the peak field strength is still reduced significantly when the period is reduced. For longer magnets as in Fig. 3.15, the maximum field is barely reduced, and the profile is still acceptable when the period S is equal to $2l_q$. All three figures show a dramatic relationship between the rms B field and the period S of the lattice. The closer together the magnets become, the rms B field decreases proportionately. In addition, the rms B field decrease is dependent on the length l_q of the magnet. This indicates that for the case of short magnets and small periodicities, the non–linear interactions of the magnetic fringe–fields on the total B field is significant. These curves are best fit by the hyperbolic tangent function to within 5% error for all the magnet parameters tested. ∇B_{max} is given by

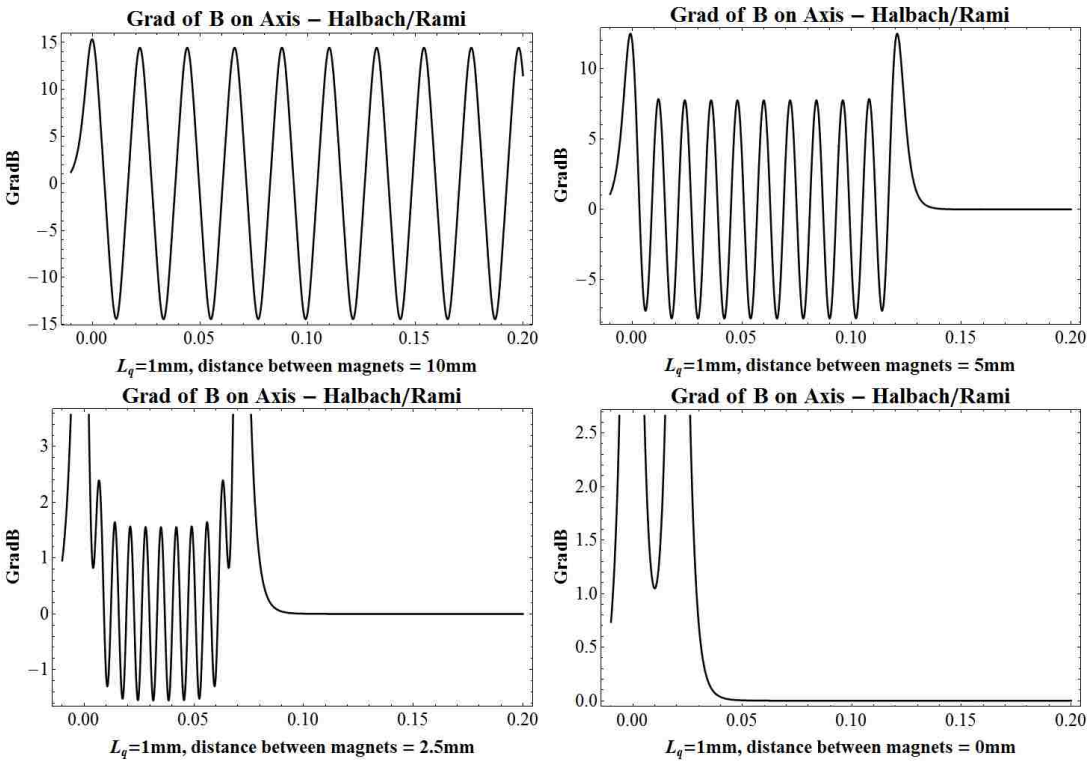

Figure 3.13: Analytic PMQ model to study multi-magnet interactions, magnet length $l_q = 1$ mm with various periods S.

$$\nabla B_{max} = S^2 \tanh(0.013\lambda_{\rm occ}). \tag{3.8}$$

We graph the peak fields for PMQ lattices vs. lattice occupancy in Fig. 3.16.

Another approximate analytic model can be constructed assuming the sinusoidal nature of the fields, and the amplitude factor obtained by Eq. 3.8 as

$$\nabla B_x \approx S^2 \tanh[0.013\lambda_{occ}] \sin\left[\left(\frac{2\pi}{S}\right) s\right], \tag{3.9}$$

where s is the direction of propagation, in this case, z. This completes the analysis of the PMQ fields for the purposes of constructing the envelope code in the following chapter. In

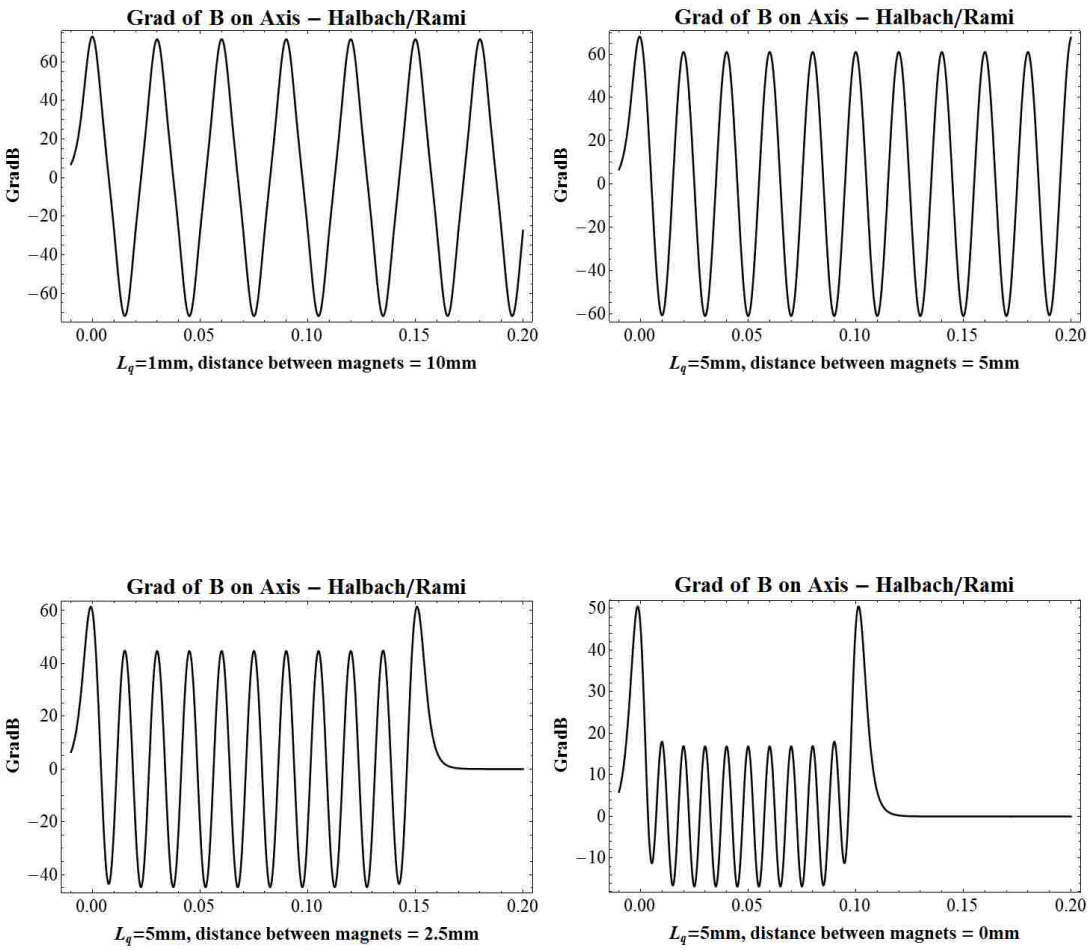

Figure 3.14: Similar to Fig. 3.13, but with larger magnet length $l_q = 5$ mm and various periods S.

the next section, we will look at an analysis of the PMQ focusing channel as performed in Reiser [23], this analysis neglects the complicated field interactions analyzed here.

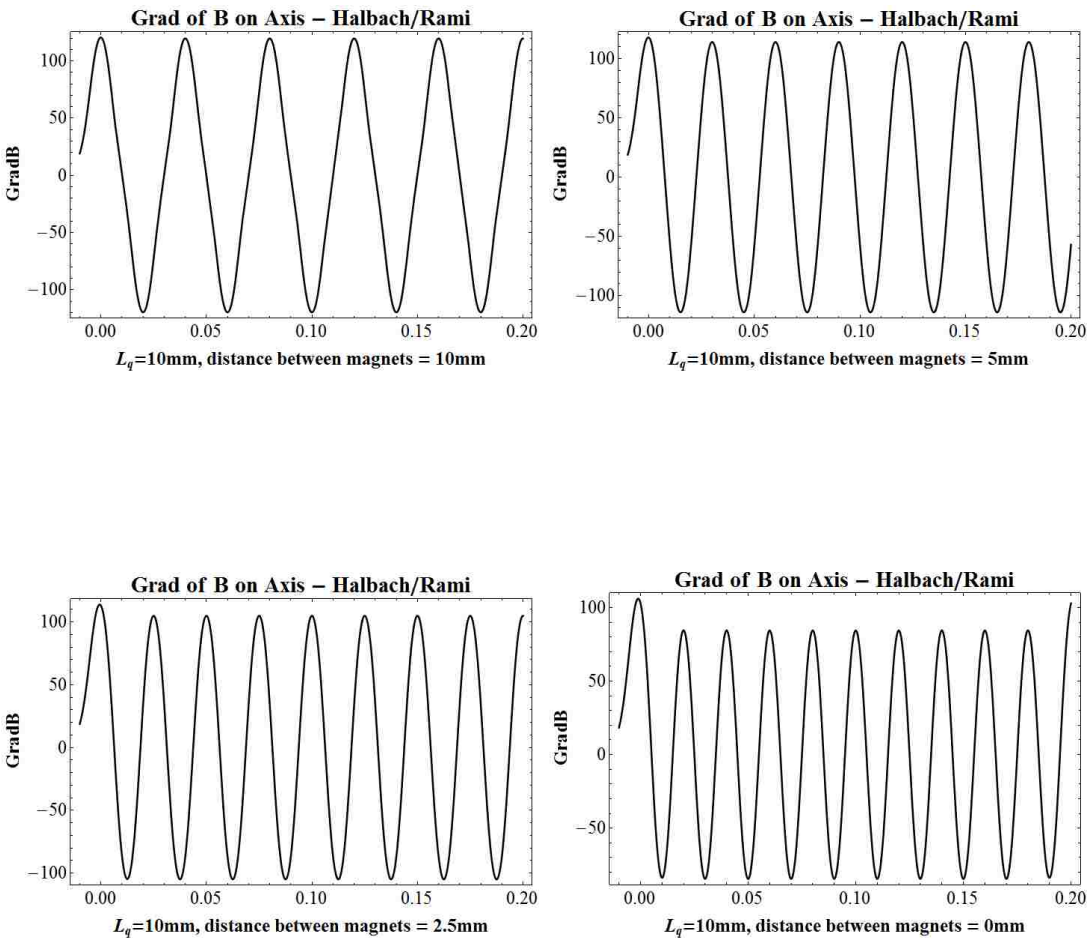

Figure 3.15: Similar to Figs. 3.13, 3.14, but with magnet length $l_q = 10$ mm and various periods S.

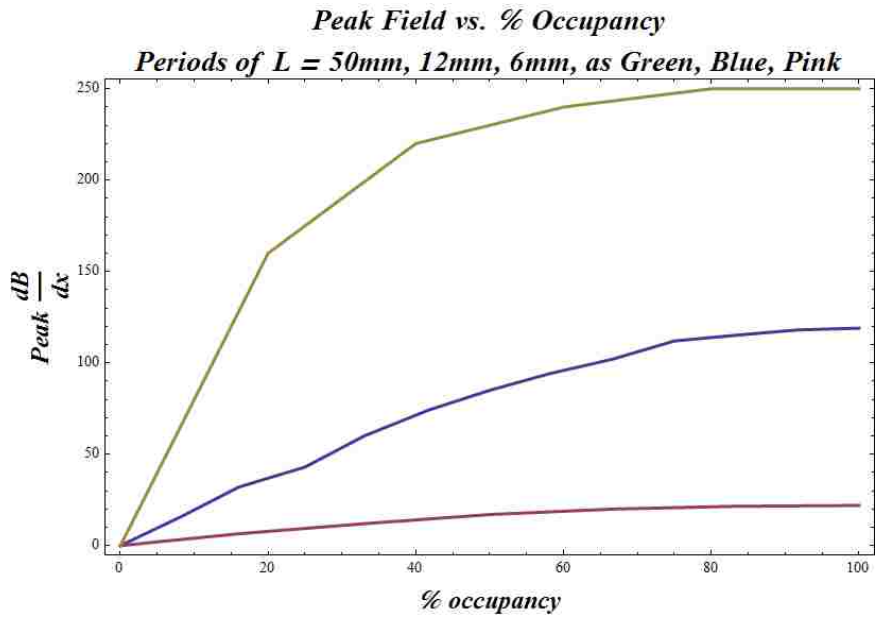

Figure 3.16: Peak magnetic fields versus magnet occupancy for PMQ lattices.

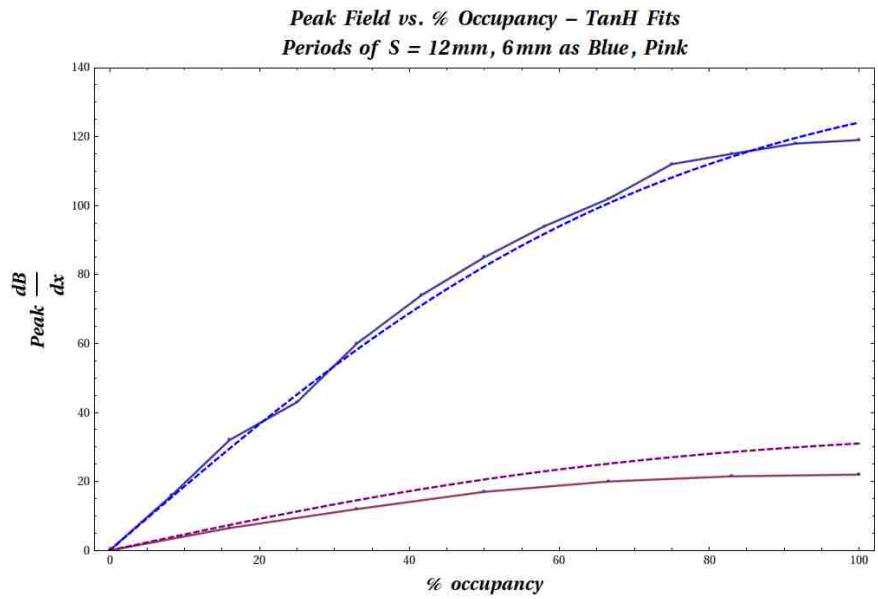

Figure 3.17: Equation 3.8, dashed lines and simulation data, solid lines.

3.4 PMQ Analysis

An analytic model of beam transport though a PMQ lattice can be performed with certain approximations which will be clearly noted. Here we derive the analytic calculation for maximum transportable current density used by [2], and used in Fig. 1.6 in Chapter 1.

We begin with the envelope equation derived from the paraxial equation with the space–charge term. We assume the mean azimuthal beam rotation in the $\vec{B}$ field is small enough that the axial self–magnetic field is negligible. Use of the paraxial ray equation assumes that the beam model is uniform, i.e. that $v/c << 1$, $\beta_r << \beta_z$, and $\beta_\theta << \beta_z$. It also demands that the generalized perveance is substantially less than unity, $|K| << 1$. Then the envelope equation using the paraxial ray equation takes the form:

$$r_m'' + \frac{\gamma' r_m'}{\beta^2\gamma} + \frac{\gamma'' r_m'}{2\beta^2\gamma} + \left(\frac{eB_{ext}}{2mc\beta\gamma}\right)^2 r_m - \left(\frac{p_\theta}{mc\beta\gamma}\right)^2 \frac{1}{r_m^3} - \frac{\epsilon_n^2}{\gamma^2\beta^2 r_m^3} - \frac{K_0}{r_m} = 0 \qquad (3.10)$$

where r_m is the maximum radial particle ray, $\epsilon_n = \beta\gamma\epsilon_{eff}$ is the normalized emittance, as will be described in more detail in Chapter 5, and K_0 is the generalized perveance also known as the space–charge term. Perveance is known as the ratio $I/V^{3/2}$, and is a common parameter in beam physics used to describe the beam. The generalized perveance K_0 is likewise proportional to $I/V^{3/2}$ in the non–relativistic limit, and proportional to $\frac{I}{\beta^3\gamma^3}$ in general. Due to the size of the quantities, perveance has units of micropervs (μpervs) which are equivalent to $\frac{A}{V^{3/2}}10^{-6}$. It is illustrative to note that the emittance term and the angular momentum term have the same $1/r^3$ dependence; both represent forces that tend to cause beam expansion. Thus, the canonical angular momentum has the same effect as the normalized emittance, and effectively increases the emittance of the beam. For this reason it is general practice to shield the cathode from the magnetic field, i.e. ensure that there is no external B field on the cathode, so that the initial canonical angular momentum of the beam is zero.

Using the analysis of beam transport in a long uniform focusing channel, we can assume that there is no applied accelerating electric field so that $\gamma' = 0$. Likewise, we can ensure that $B = 0$ at the cathode so that the canonical angular momentum p_θ goes to zero. It is

then possible to rewrite the paraxial ray equation as the envelope equation:

$$r[s]'' + k_0 r[s] - \frac{K_0}{r[s]} - \frac{\epsilon_{eff}^2}{r[s]^3} = 0 \tag{3.11}$$

where k_0 is the external magnetic focusing force. Reiser [23] shows in section 4.4 that in the *smooth approximation*, where only average forces are considered, a quadrupole periodic–focusing channel behaves like solid cylinder filled with opposite charge around the beam. Mathematically, the average behavior of the particle motion, or beam envelope, in a periodic quadrupole lattice is identical to that of particle transport through a stationary cylinder of opposite charge with uniform density ρ_e.

The radial E field due to a uniform charge distribution of density ρ_e is

$$E_r = \frac{\rho_e r}{2\epsilon_0}. \tag{3.12}$$

Equation 3.11 must have one solution where $r[s] = a = constant$, $r'[s] = 0$, $r''[s] = 0$. This case is what we call a matched beam, and Eq. 3.11 reduces to

$$k_0^2 a - \frac{K_0}{a} - \frac{\epsilon_{eff}^2}{a^3} = 0. \tag{3.13}$$

If we allow space–charge to be negligible for the moment, then $K_0 = 0$ and we can solve Eq. 3.13 for a beam radius we call a_0 and define $a_0 = \left(\frac{\epsilon_{eff}}{k_0}\right)^2$. For the case of the matched beam, we can replace the emittance term as $\epsilon_{eff} = \alpha$ where $\alpha = k_0 a_0^2$ and a_0 is the average beam radius.

Solving for K_0 and rewriting Eq. 3.13 in terms of the parameter α as, we obtain

$$K_0 = k_0^2 a^2 - \frac{\epsilon_{eff}^2}{a^2} = k_0 a \left(1 - \frac{\epsilon_{eff}}{\alpha}\right)^2\Bigg). \tag{3.14}$$

Setting Eq. 3.14 equal to the space–charge term as defined by Lawson [24], we obtain

$$K_0 = \frac{2I}{I_0 \beta^3 \gamma^3} = k_0 \left(1 - \left(\frac{\epsilon_{eff}}{\alpha}\right)^2\right), \tag{3.15}$$

and solving for current I we obtain

$$I = \frac{I_0}{2}(\beta\gamma)^3 k_0 \alpha \left(1 - \left(\frac{\epsilon_{eff}}{\alpha}\right)^2\right). \tag{3.16}$$

To arrive at a useful equation for the PPM lattice design, we need to substitute α with $k_0 a_0^2$, and rewrite k_0 in terms of the phase advance σ. Phase advance, σ, is defined by $\sigma = \frac{2\pi S}{\lambda}$, where S is the period of the focusing lattice, and $k = \frac{2\pi}{\lambda}$ or $k_0 = \frac{2\pi}{\lambda_0}$. Hence

$$\sigma_0 = \frac{2\pi}{\lambda_0}, \text{and } k_0 = \frac{\sigma_0}{S}. \tag{3.17}$$

We can replace α in Eq. 3.16 with

$$\alpha = \frac{\sigma_0}{S} a_0^2, \tag{3.18}$$

and obtain

$$S = \sigma_0 \left(\frac{2I}{a_0^2 I_0 \beta^3 \gamma^3} - \left(\frac{\epsilon_{eff}}{a_0^2}\right)^2\right)^{-1/2}. \tag{3.19}$$

Equation 3.19 is the main design equation used to show a strong advantage for current density transport using PMQ lattices over PPM lattices. If it is solved for current density, we recover Eq. 1.5. In the next chapter the difference between this theoretical calculation for determining the maximum transportable current density and the maximum transportable current density determined from envelope calculations using the magnet model developed in the previous section will be compared.

Chapter 4

Development of Envelope Codes

Envelope codes are very useful tools to develop designs of magnet lattices for electron beam focusing. The beam envelope follows the trajectory of the outermost electron in a beam. For accurate envelope calculations, we assume a laminar beam, i.e., the trajectories of the electrons in the beam do not cross; this ensures that the electron trajectory we follow does represent the entire beam. Standard envelope codes like Trace 3-D [13] are available; however, most of these codes only have hard–edge quadrupole models in them. In order to more accurately account for the fringing fields and the multi-magnet interactions, we developed our own envelope codes using the field models developed in the previous two chapters. First, we developed the PPM envelope code and used it to verify our method by comparing it with well-known design equations for PPM current density transport. We then developed the envelope code for beams traversing PMQ lattices.

Both envelope codes were developed with the same methodology, which is outlined as follows:

1. Develop an analytic magnetic field model for the magnet lattice, as discussed in Chapters 2, 3.

2. Solve the equations of motion (Lorentz force law) for single particle motion.

3. Calculate the zero-current phase advance σ_0 using the period of the single particle trajectory.

4. Add Lawson's space–charge term, K_0, to account for multi-particle physics.

5. Solve the nonlinear differential equations using the standard differential equation solver in *Mathematica*.

6. Match the beam at the highest phase advance possible to determine maximum transportable current density per lattice. Beam matching is performed by adjusting the initial conditions in the differential equation solver.

4.1 Derivation of the Envelope Equation

The Distribution Function

To derive the envelope equation that we use in Chapter 3, we must start with the particle distribution function. The distribution of N particles in phase space can be written as:

$$f(\overrightarrow{x}, \overrightarrow{p}) = \sum_{i=1}^{N} \delta^3(\overrightarrow{x} - \overrightarrow{x_i})\delta^3(\overrightarrow{p} - \overrightarrow{p_i}) \tag{4.1}$$

where $\delta^3(\overrightarrow{x} - \overrightarrow{x_i})\delta^3(\overrightarrow{p} - \overrightarrow{p_i})$ is the product of two three-dimensional Dirac delta-functions to indicate each particle position in six dimensional phase space: $(\vec{x_i}, \vec{p_i})$, where each $\vec{x_i}$ represents a particle's position, and each $\vec{p_i}$ represents a particle's momentum.

The full distribution function contains all the information needed to describe the state of the non–interacting beam particles. If we view it as a continuous function, which allows us to ignore higher-order microscopic interactions, the distribution evolution can be described by the well-known Vlasov equation:

$$\frac{df}{df} + \dot{\overrightarrow{x}} \cdot \overrightarrow{\nabla_{\overrightarrow{x}}} f + \dot{\overrightarrow{p}} \cdot \overrightarrow{\nabla_{\overrightarrow{p}}} f = 0. \tag{4.2}$$

A theoretical model that satisfies Eq. 4.2 is the distribution of Kapchinsky and Vladimirsky, known as the K–V distribution [25]. The K–V distribution can be defined as a delta function of the transverse emittances, and is consistent with the distribution function we gave above as Eq. 4.1. The K–V beam has the property that the density profile is uniform with sharp boundaries. Since the self–fields of a uniform density beam are linear with position s, the density remains uniform and sharply bounded as the beam propagates through linear focusing systems. This is the typical distribution associated with beam envelopes.

For a description of the distribution evolution that will lead to the envelope equation, one can take *moments* of the distribution, which are defined by

$$\int_{-\infty}^{\infty}\int_{-\infty}^{\infty} x^n p_x^m f(x, p_x) dx dp_x, \tag{4.3}$$

where n, m are zero or positive integers, and the quantity $n + m$ is called the order of the moment. This description currently employs the transverse phase plane $(\overrightarrow{x_i}, \overrightarrow{p_i})$. We want to use equivalent trace space (x, x'). The moments in equivalent trace space are defined by

$$\int_{-\infty}^{\infty}\int_{-\infty}^{\infty} x^n (x')^m f_x(x, x') dx dx'. \tag{4.4}$$

To use the equivalent trace space we replace the momentum with the angle x' in phase plane plots.

The zeroth-order moment in trace space is just the normalization condition on the distribution function:

$$\int_{-\infty}^{\infty}\int_{-\infty}^{\infty} f_x(x,x')dxdx' = 1. \tag{4.5}$$

The first-order moments are called the centroids of the distribution:

$$\langle x\rangle = \int_{-\infty}^{\infty}\int_{-\infty}^{\infty} x f_x(x,x')dxdx', \tag{4.6}$$

$$\langle x'\rangle = \int_{-\infty}^{\infty}\int_{-\infty}^{\infty} x' f_x(x,x')dxdx'. \tag{4.7}$$

Physically, the first-order moments go to zero when the beam is aligned to its design axis. The second order moments are:

$$\sigma_{x^2} = \langle x^2\rangle = \int_{-\infty}^{\infty}\int_{-\infty}^{\infty} x^2 f_x(x,x')dxdx', \tag{4.8}$$

$$\sigma_{x'^2} = \langle x'^2\rangle = \int_{-\infty}^{\infty}\int_{-\infty}^{\infty} x'^2 f_x(x,x')dxdx', \tag{4.9}$$

and

$$\sigma_{xx'} = \langle xx'\rangle = \int_{-\infty}^{\infty}\int_{-\infty}^{\infty} xx' f_x(x,x')dxdx', \tag{4.10}$$

where, physically, σ_x is the rms beam width, $\sigma_{x'}$ is the rms momentum width, and $\sigma_{xx'}$ indicates the degree of correlation between x and x'. We are interested in the evolution of the second moments of the distribution function because they determine the evolution of the trace space distribution of the beam.

RMS Envelope Equation

The standard formalism for including non-trivial beam self-forces and external focusing forces is by use of an envelope analysis. As such, we will develop what is called the rms beam envelope equation. To begin, we write the first derivative of the rms beam radius derived in the previous section as

$$\frac{d\sigma_x}{dz} = \frac{d}{dz}\sqrt{\langle x^2 \rangle} = \frac{1}{2\sigma_x}\frac{d}{dz}\langle x^2 \rangle, \tag{4.11}$$

$$= \frac{1}{2\sigma_x}\frac{d}{dz}\int_{-\infty}^{\infty}\int_{-\infty}^{\infty} x^2 f_x(x,x')dxdx', \tag{4.12}$$

$$= \frac{1}{\sigma_x}\int_{-\infty}^{\infty}\int_{-\infty}^{\infty} xx' f_x(x,x')dxdx', \tag{4.13}$$

$$= \frac{\sigma_{xx'}}{\sigma_x}. \tag{4.14}$$

Using this relationship, we can take the second derivative of the envelope equation as

$$\frac{d^2\sigma_x}{dz^2} = \frac{d}{dz}\frac{\sigma_{xx'}}{\sigma_x}, \tag{4.15}$$

$$= \frac{1}{\sigma_x}\frac{d\sigma_{xx'}}{dz} - \frac{\sigma_{xx'}^2}{\sigma_x^3}, \tag{4.16}$$

$$= \frac{1}{\sigma_x}\frac{d}{dz}\int_{-\infty}^{\infty}\int_{-\infty}^{\infty} xx' f_x(x,x')dxdx' - \frac{\sigma_{xx'}^2}{\sigma_x^3}. \tag{4.17}$$

Applying the chain-rule we obtain

$$= \frac{\langle x'^2 \rangle + \langle xx'' \rangle}{\sigma_x} - \frac{\sigma_{xx'}^2}{\sigma_x^3}, \tag{4.18}$$

$$= \frac{\left(\sigma_{x'}^2 + \langle xx'' \rangle\right)\sigma_x^2}{\sigma_x^3} - \frac{\sigma_{xx'}^2}{\sigma_x^3}. \tag{4.19}$$

Upon rearranging:

$$\sigma_x'' = \frac{\sigma_x^2\sigma_{x'}^2 - \sigma_{xx'}^2}{\sigma_x^3} + \frac{\langle xx'' \rangle}{\sigma_x^3}. \tag{4.20}$$

Let $\sigma_x^2\sigma_{x'}^2 - \sigma_{xx'}^2$ be called $\epsilon_{x,rms}^2$.

Then we can rewrite the last equation as:

$$\sigma_x'' = \frac{\epsilon_{x,rms}^2}{\sigma_x^3} + \frac{\langle x x'' \rangle}{\sigma_x}. \tag{4.21}$$

From optics, the deflection from an external linear focusing force as a ray description is

$$x'' + \kappa^2 x = 0. \tag{4.22}$$

where Eq. 4.22 is the equation of single particle motion with some external focusing force, κ^2. Substituting Eq. 4.21 into Eq. 4.22, we obtain:

$$\sigma_x'' + \kappa_x^2 \sigma_x - \frac{\epsilon_{x,rms}^2}{\sigma_x^3} = 0. \tag{4.23}$$

Electron Self-Fields

To add the force due to the electron self–fields, we will assume a laminar beam with uniform charge density ρ_o. Since space–charge gives rise to a radial force and depends on current density we derive the equations of motion with a term corresponding to space-charge.

The charge density for a continuous uniform cylindrical beam is defined by:

$$\rho(z) = \begin{cases} \rho_0, & \text{for } r \leq r_a \\ 0, & \text{for } r > r_a \end{cases} \tag{4.24}$$

where r_a is the beam edge radius.

The self-forces of the electrons are derived using the radial Lorentz force law,

$$F_r = e(E_r - \beta c B_\theta). \tag{4.25}$$

We are assuming that the paraxial assumption holds (i.e. particle velocities $v_r, v_\theta << v_z \approx v$), and that the difference in potential energy across the beam is small compared to the kinetic energy of the beam. The charge density of the beam is related to the beam current by the continuity equation, such that:

$$\rho_0 = \frac{I}{\pi r_a^2 v}. \tag{4.26}$$

The electric field can be found from Gauss's Law as

$$\oint_S \epsilon_0 \vec{E} \cdot d\vec{S} = \int_v \rho_0 dV, \tag{4.27}$$

$$2\pi r l \epsilon_0 E_r = \rho_0 \pi l r^2 \rightarrow E_r = \frac{\rho_0 r}{2\epsilon_0} \text{ for } r \leq a. \tag{4.28}$$

Similarly, B_θ can be found from Ampere's Law as

$$\int \vec{B} \cdot dl = \mu_0 \oint_S \vec{J} \cdot d\vec{S}, \tag{4.29}$$

$$2l\pi B_\theta = \mu_0 J l r \rightarrow B_\theta = \frac{\mu_0 J r}{2} = \frac{\mu_0 r I}{2\pi r_a^2} \text{ for } r \leq a. \tag{4.30}$$

Substituting $c = \sqrt{\frac{1}{\mu_0 \epsilon_0}}$, and $B_\theta = \frac{\beta}{c} E_r$ into the radial Lorentz Force Law, we obtain

$$F_r = e(E_r - \beta c B_\theta) = e(1 + \beta^2) E_r = \frac{e E_r}{\gamma^2}, \tag{4.31}$$

$$F_r = \frac{e}{\gamma^2} \frac{\rho_0 r_a \hat{r}}{2\epsilon_0}, \tag{4.32}$$

$$m \frac{d^2 r}{dt^2} = \frac{|e| r}{2\gamma^2 \epsilon_0} \frac{I}{\pi r_a^2 v}. \tag{4.33}$$

Dividing by m, and transforming from dt to dz using $\frac{d^2r}{dt^2} = \beta^2 c^2 \frac{d^2r}{dz^2}$ we obtain

$$\frac{d^2r}{dz^2} = \frac{|e|Ir}{2\pi\gamma^3 v^3 m\epsilon_0 r_a^2}, \tag{4.34}$$

where

$$K_0 = \frac{|e|I}{2\pi\gamma^3 v^3 m\epsilon_0}. \tag{4.35}$$

Including this term in the envelope equation derived earlier, and accounting for the two planes of symmetry x–z, y–z we arrive at the full envelope equations

$$x''[s] + \kappa_x x[s] - \frac{2K_0}{x[s]+y[s]} - \frac{\epsilon_{x,rms}^2}{x[s]^3} = 0, \tag{4.36}$$

and

$$y''[s] + \kappa_y y[s] - \frac{2K_0}{x[s]+y[s]} - \frac{\epsilon_{y,rms}^2}{y[s]^3} = 0. \tag{4.37}$$

It is easy to show that these space–charge force terms satisfy Poisson's Equation.

4.2 PPM Envelope Code

The PPM envelope code employs the general envelope equation:

$$r'' + \kappa_{ppm} r - \frac{K_0}{r} = 0, \tag{4.38}$$

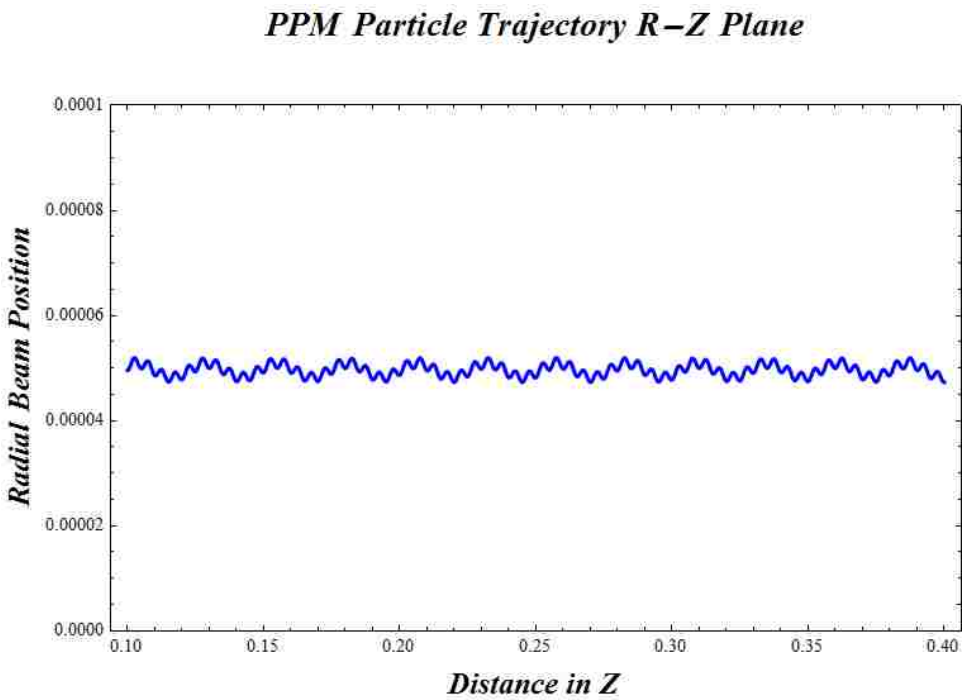

Figure 4.1: PPM envelope demonstrating stable transport.

where

$$\kappa_{ppm} = \frac{\frac{e}{m} B_{ppm}^2}{8V_k}, \tag{4.39}$$

B_{ppm} is the magnetic field developed in Chapter 2 and V_k is the beam voltage. K_0 is Lawson's space–charge term, also known as the electron self–field term and the generalized perveance and is fully relativistic. It is given by

$$K_0 = \frac{q_e I_0}{2\pi\epsilon_0 c^3 \beta^3 \gamma^3}. \tag{4.40}$$

Solving Eq. 4.38 using the numerical differential solver in *Mathematica* gives the beam envelope trajectory in Fig. 4.1.

Figure 4.1 shows stable beam transport with the small oscillations matching the focusing periodicity. The larger oscillations demonstrate a very slight mismatch of the beam. Simulations were performed for a variety of lattice parameters, in particular varying the lattice period. The matched beam was found for each case and the amount of current

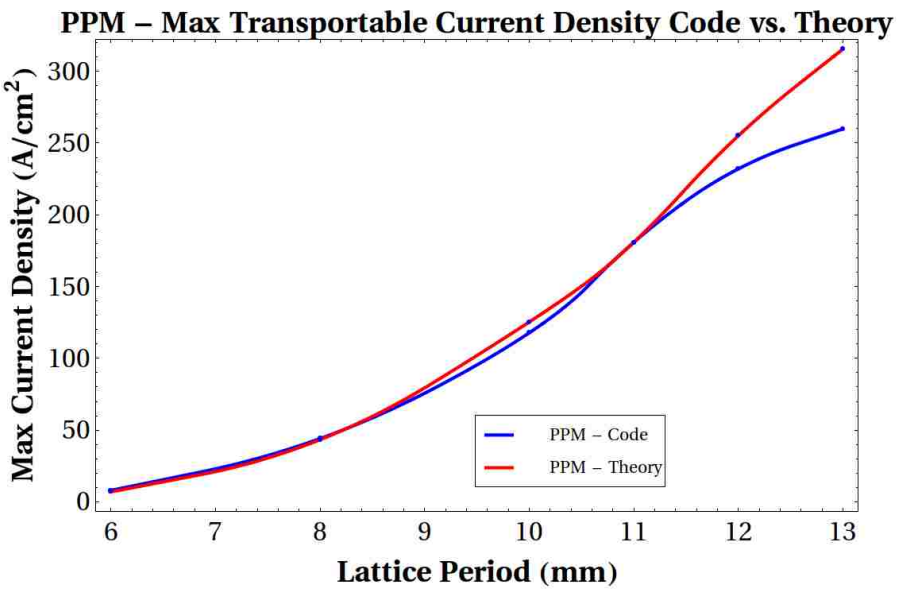

Figure 4.2: Verification of the PPM envleope code to theory.

density in the matched beam per lattice period S is presented in Fig. 4.2. Results from the PPM envelope code are shown with theoretical PPM calculations based on the commonly used Sterrett-Heffner PPM design formula from [20]. This agreement is considered very good; there is slight divergence from the theoretical curve when we get to large lattice periods which should be due to the inclusion of iron pole piece effects in the Sterrett-Heffner equations. The regime we are particularly concerned with is limited to the smaller lattice periods.

We did add an emittance term to the PPM envelope equation analyzed and for low emittances, e.g. $\epsilon_{eff} \approx 0.1$ π-mm-mrad, saw no difference in the trajectories or transportable current density.

4.3 PMQ Envelope Code

Having verified the envelope code methodology for the PPM envelope equation, a similar envelope code was developed with the PMQ magnetic field model developed and verified in Chapter 3. The PMQ envelope code, including space-charge effects, was developed with a full fringing field model of the Halbach 16-piece quadrupole magnets. Each PMQ lattice was optimized using the envelope code to obtain the maximum current density transportable for a given beam energy and appropriate magnet dimensions.

For this work, lattice parameters appropriate for transporting a beam in a 30 GHz coupled-cavity TWT were chosen. The beam energy is varied from 16 keV to 50 keV, the mean beam radius is ≈ 0.5 mm, and the inner and outer magnet dimensions are fixed at $r_i = 4$ mm and $r_o = 12$ mm. The lattice period S is varied.

4.3.1 Single Particle Tracking

Single particle tracking is performed to ensure that the beam remains stable according to the Mathieu stability conditions. Single particle tracking uses the Lorentz equation of motion and tracks the trajectory of a single electron traversing a magnetic focusing lens, or lattice of lenses in this case. The beam is determined to be stable when the zero-current phase advance σ_0 is less than 90 degrees [23]. Since the quadrupole focused beam has two planes of symmetry, two coupled equations of motion are required. The equations of motion from the Lorentz force law for an electron traveling though a focusing force with two planes of symmetry are

$$\gamma m x'' = e v_z B_y \;\text{ and }\; \gamma m y'' = -e v_z B_x. \tag{4.41}$$

In our case the focusing force is generated by a 16–piece Halbach quadrupole lattice with $B_y = \frac{dB}{dy}x$, and $B_x = \frac{dB}{dx}y$ where $\frac{dB}{dy} = \frac{dB}{dx}$. We can therefore replace B_x and B_y with their gradient multiplied by y and x respectively. The equations of motion then become

$$x'' + \frac{q v_z}{\gamma m_e}\frac{dB}{dx}x = 0 \text{ and } \; y'' - \frac{q v_z}{\gamma m_e}\frac{dB}{dx}y = 0. \tag{4.42}$$

Thus, as the beam traverses one element, we get focusing in one plane and defocusing in the other. Now we can eliminate time and rewrite these equations of motion as trajectory equations letting $z = v_z t \approx v \approx$ constant, and $\frac{d^2}{dt} = v^2 \frac{d^2}{dx^2}$. Then Eqs. 4.42 become Eq. 4.43 and Eq. 4.44. These equations are solved with the full magnetic field profile of the quadrupole lattice, Eq. 3.1, from Chapter 3. The equations give the position of the particle in the x–z and the y–z planes as

$$x''[s] + \kappa_x x[s] = 0 \tag{4.43}$$

and

$$y''[s] + \kappa_y y[s] = 0, \tag{4.44}$$

where

$$\kappa_x = \frac{e\frac{dB}{dx}[s]}{\gamma mc\beta}, \tag{4.45}$$

and $\kappa_x = -\kappa_y$. Equations 4.43, 4.44 were solved using the standard differential equation solver in *Mathematica* [26], the solutions of the particle motion for each plane is seen in Fig. 4.3. To determine stability, it is necessary to determine the phase advance of the particle motion. A sinusoidal curve fit was used to determine the period of the particle trajectory. The particle trajectory in x–z plane is shown in Fig. 4.4 with a sinusoidal curve fit. The period of the particle trajectory is then used to determine the phase advance per lens, σ_0 from Eq. 3.17. To maintain a stable beam while transporting maximum current, σ_0 is kept as close to 90 degrees as possible without exceeding it. For comparison with theory, a lattice with no overlapping fringing fields was selected and the phase advance determined by envelope simulations was compared to the phase advance determined analytically using the hard-edge quadrupole approximation from Eq. (3.354) in [23]. Equation (3.354) is reproduced here as

$$\sigma_0 = \cos^{-1}[\cos\theta\cosh\theta + \frac{L\theta}{l} * (\cos\theta\sinh\theta - \sin\theta\cosh\theta)], \tag{4.46}$$

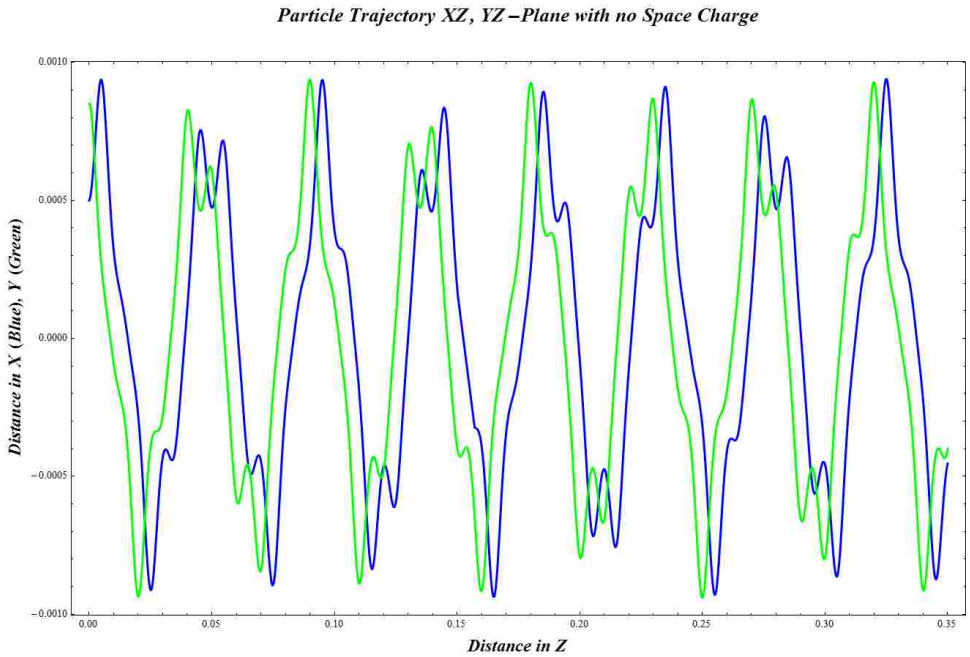

Figure 4.3: Single particle tracking in the x–z plane (green) and the y–z (blue) plane.

where θ represents the focusing strength of the lenses and is defined by $\theta = (\kappa_{x,y})^2 \, l_q$. For the lattice shown in Fig. 3.3, with $l = 1.9$ mm and $\frac{L}{2} - l = 5$ mm, the phase advance as calculated using Eq. 4.46 is 58.7 degrees, and the phase advance derived from the particle tracking is 64 degrees. This is within the standard error for the hard-edge quadrupole model.

4.3.2 Space-Charge Effects

The maximum transportable current density can be found by including space-charge effects in the single particle tracking calculation. The equations of motion then become the envelope equations. Since the space–charge term is a function of current, the maximum current density transportable for a given PMQ lattice can be determined by incrementally increasing the current density until the depressed phase advance, the phase advance of the beam envelope with space–charge, goes to zero. Thus, the larger the phase advance up to

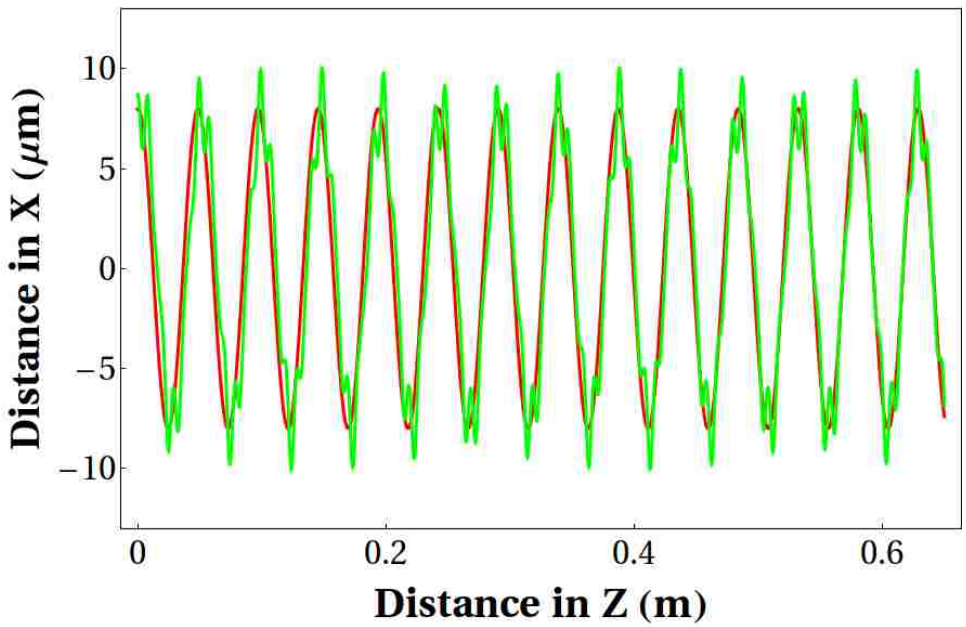

Figure 4.4: The particle trajectory in the x–z plane (green) and a period fitting function (red).

90°, the higher the transportable current density.

Space–charge effects were accounted for by including the space-charge term [24] in Eqs. 4.43, 4.44. This results in two coupled nonlinear second order differential equations:

$$x''[s] + \kappa_x x[s] - \frac{2K_0}{x[s] + y[s]} = 0 \tag{4.47}$$

and

$$y''[s] + \kappa_y y[s] - \frac{2K_0}{x[s] + y[s]} = 0, \tag{4.48}$$

where K_0 is the generalized perveance and a function of the beam current. Solving Eqs. 4.47, 4.48 allows for the calculation of the depressed phase advance. When the depressed phase advance goes to zero degrees, the beam is matched and the current density transported is maximized. Profiles of the beam envelope for unmatched and matched beams are

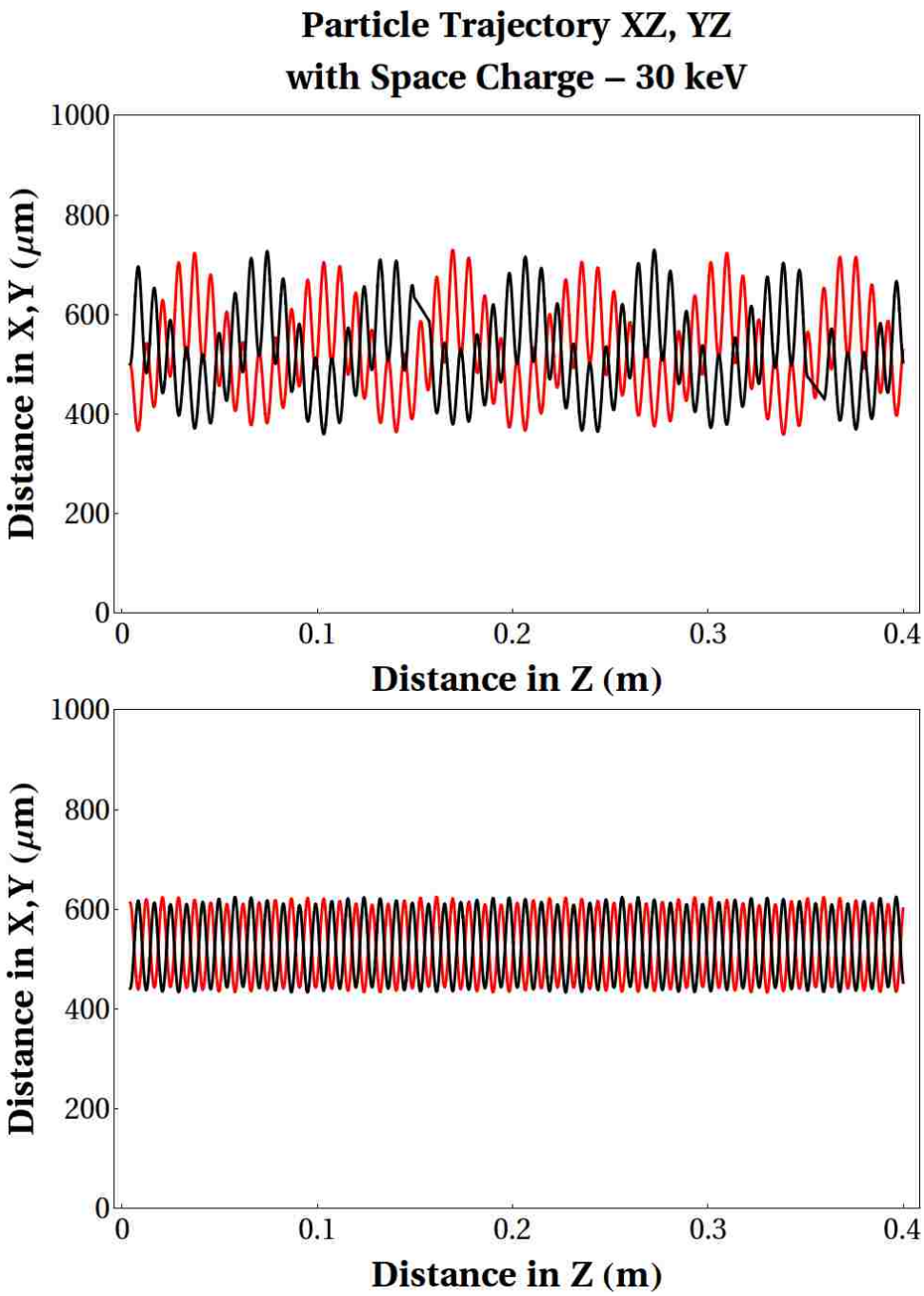

Figure 4.5: The x–z particle trajectory (black) and the y–z particle trajectory (red). Top: for the case of an unmatched beam; bottom: for the case of a matched beam.

shown in Fig. 4.5. Similar to the PPM envelope trajectory, the small oscillations represent the particles moving through a single set of quadrupole magnets showing the defocusing and refocusing of the beam-edge, the periodicity of the oscillations matching that of the magnet lattice. The large oscillations are artifacts from the unmatched conditions, known in the accelerator community as betatron oscillations. Beam matching is performed by adjusting the parameters a through d in $x[0] = a$, $y[0] = b$, $x'[0] = c$, $y'[0] = d$.

4.3.3 Stability and Optimization

Optimization of the lattices required parameter scans of different magnet occupancies for each lattice period. For each period, simulations were performed calculating the phase advance and the maximum transportable current density for each matched beam. Results from one lattice optimization are presented in Table 4.1 for a 50 keV electron beam with magnet dimensions $r_i = 4$ mm and $r_o = 12$ mm.

Table 4.1: Current Density Transportable per Occupancy– Period $S = 11$ mm.

Occupancy λ_{occ}	Phase advance σ_0	Max Current Density
4.16%	4.46°	4.2 A/cm^2
8.33%	9.82°	15.8 A/cm^2
12.5%	16.11°	32.6 A/cm^2
16.6%	22.91°	53.8 A/cm^2
20.83%	30.68°	77.8 A/cm^2
25.00%	39.19°	103.2 A/cm^2
29.16%	48.44°	130.3 A/cm^2
33.33%	58.7°	159.3 A/cm^2
37.50%	69.48°	186.3 A/cm^2
41.60%	82.84°	214.6 A/cm^2
45.83%	95.87°	unstable
50.00%	112.75°	unstable

It is evident from Table 4.1 that a certain magnet occupancy is optimal for transporting the most current density for a given lattice period S, too much magnetic field creates unstable transport. For smaller lattice periods, even 100% occupancy cannot achieve a sufficient phase advance for transporting large current densities, this can be seen in Table

4.2. Phase advance is the crucial stability factor for PMQ focusing and transport, and it creates two distinct regions, a region where the phase advance is limited by magnet dimensions and is too low to transport sufficient current densities, and a region where the phase advance is nearly 90° and the magnet occupancy decreases as the periodicity is increased. This second region is where the size and weight advantage of PMQ over PPM can clearly be seen. Both size and weight are proportional to λ_{occ}.

Table 4.2: Occupancy and Phase Advance for various S, 25 keV beam.

S	l_q	Occupancy λ_{occ}	Phase advance σ_0	Max J
2 mm	1.0 mm	100%	3.89°	0.09 A/cm^2
3 mm	1.5 mm	100%	13.40°	0.51 A/cm^2
4 mm	2.0 mm	100%	30.90 °	5.54 A/cm^2
5 mm	2.5 mm	100%	61.59°	63.66 A/cm^2
6 mm	2.5 mm	90%	86.85°	57.0 A/cm^2
7 mm	2.0 mm	57%	86°	43.0 A/cm^2
8 mm	1.3 mm	32.5%	86°	38.0 A/cm^2
9 mm	1.1 mm	24.4%	86°	32.0 A/cm^2
10 mm	0.85 mm	17%	86°	23.0 A/cm^2

4.3.4 Maximum Transportable Current Density

The maximum transportable current density through a PMQ lattice was determined for the limiting factors of beam energy and inner magnet radius. The outer radius of the magnets can be made as large as needed to reach the asymptotic value of magnetic field intensity without being unreasonably large. As such, the outer magnet radius is not a limiting factor in transportable current density. For an inner magnet radius of 4 mm, the current density as a function of period is optimized. Optimization was performed by varying the magnet width l_q and the space between magnets in the single-particle-tracking code to obtain the zero-current phase advance as close to 90 degrees as possible. As the lattice period becomes small, the beam cannot achieve 90 degrees phase advance for any magnet thickness, resulting in the drop off in maximum current density observed in Fig. 4.6, but not seen in Fig. 1.6. In Fig. 4.6 the black curve represents the 16 keV beam,

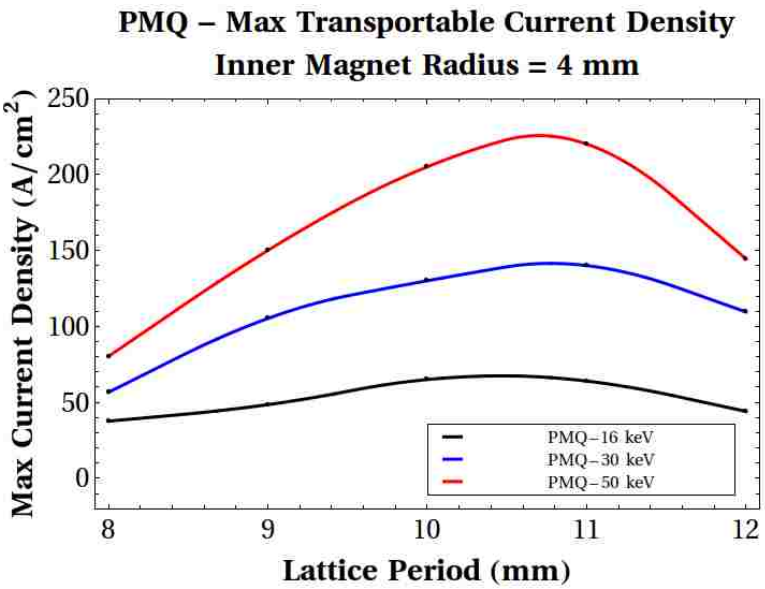

Figure 4.6: Maximum transportable current density optimized per lattice period for the beam energies indicated.

which is comparable to the black curve in Fig. 1.6. The maximum transportable current density for various reasonable values of beam energy are presented in Fig. 4.6.

It is worth noting that for a single case, stable beam transport using a PMQ lattice for a space–charge dominated beam has been simulated using the 3D particle-in-cell code MICHELLE [14], [27] in [2]. Results from the envelope code agree with these simulation results, however, their predictions for other cases were based on the analytic PMQ transport model.

If we compare our results to the analytic PMQ transport model, we see a drastic difference for small lattice periods. The analytic model does not take into account the drop–off of the field due to small lattice periods, as well as the low phase advance achievable for small periods. This can clearly be seen in Fig. 4.7. It is important to note that the maximum current density transportable that was calculated used a maximum beam radius size instead of an average beam radius size. The theoretical calculations did use an average beam radius size, so the comparisons are not perfect, they are a modest approximation.

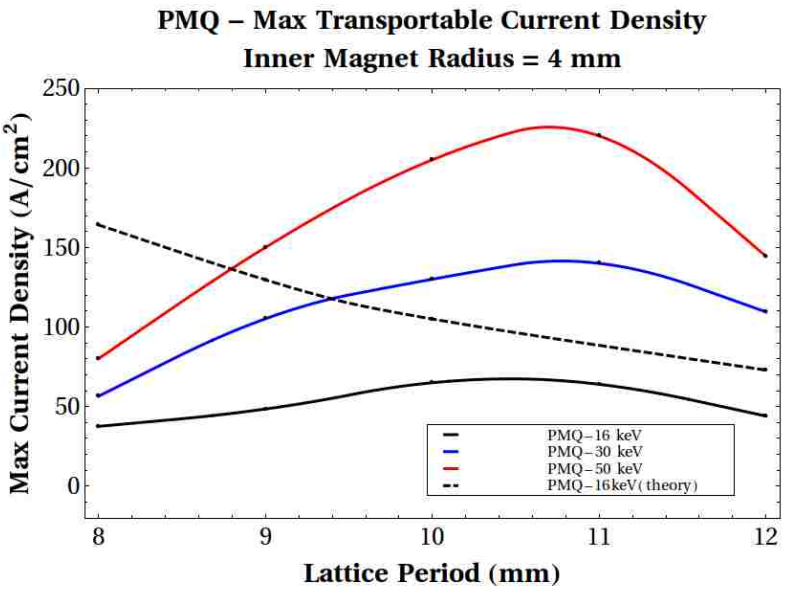

Figure 4.7: Maximum transportable current density from envelope calculations versus analytic transport model.

4.3.5 Emittance

For completeness, we added an initial emittance term to the simulations assuming a cathode temperature of 1100°. The envelope equations then become

$$x''[s] + \kappa_x x[s] - \frac{2K_0}{x[s]+y[s]} - \frac{\epsilon^2_{eff-x}}{(x[s]+y[s])^3} = 0 \tag{4.49}$$

and

$$y''[s] + \kappa_y y[s] - \frac{2K_0}{x[s]+y[s]} - \frac{\epsilon^2_{eff-y}}{(x[s]+y[s])^3} = 0. \tag{4.50}$$

Results for the emittance emittance studies were similar to what was obtained before with the equations of motion with space–charge, a slightly stronger focusing force was required to achieve stable transport, but only very slightly; the same current density per phase advance was achieved for beams of moderate radius, $a_0 = 0.5$ mm. For smaller radii, a larger difference was noted but not quantified here.

Chapter 5

Emittance Growth in Transport Lattices

Emittance increasingly becomes an issue for high-frequency RF amplifiers as dimensions become minute. This is currently an active area of research with articles being published in 2014 to address designing emittance dominated beams for linear RF amplifiers [28]. Emittance growth, on the other hand, has never been thought to be an issue for RF amplifiers. In this section, we develop a method for determining the emittance growth that can be caused by PPM focusing lattices. This can be used as a tool for determining important beam related design issues in RF amplifiers.

5.1 Beam Emittance

The source of the electron beam is the electron gun, consisting of a piece of metal (cathode) from which electrons are born and accelerated across a potential difference between the cathode and anode, and emerge through a hole in the anode. Electrons are produced on the cathode by various means: the cathode can be heated – thermionic emission, the cathode can be cold and solely use the potential between the anode and cathode to induce

emission of electrons – field emission, or the cathode can be bombarded with photons to induce emission – photoemission. Whatever the method of emission, the nature of the source causes an initial kinetic energy spread, and a random velocity spread, of the electrons in the beam. Each electron is born with a slightly different direction and magnitude of velocity - this random velocity spread is proportional to the initial temperature of the cathode and causes an intrinsic thermal velocity spread which remains with the beam at any distance from the cathode. The intrinsic thermal velocity spread, also called the random velocity spread, can be increased by temperature fluctuations on the cathode itself, aberrations due to space–charge fields, and various other instabilities. The greater and the less uniform the initial energy and velocity spreads are, the poorer the beam quality is. *Emittance* is a measure of the beam quality.

The two beams of interest for us are the axisymmetric case of the PPM focused beam, and the two–plane symmetry of the PMQ focused beam. We will focus on the two–plane case which reduces to the axisymmetric case. In phase space, each particle can be described by its three spatial coordinates and three momentum coordinates (x, y, z, P_x, P_y, P_z) at any given time. A collection of particles is considered a beam if its momentum in one dimension is much greater than its momentum in the other two dimensions; namely, in a particle beam moving along the z axis, $P_z >> P_x, P_y$. Considering the symmetric case of a PMQ focused beam, we have particles traveling in the x–z and in the y–z planes. The slope of the trajectory of the particle in the x–z plane is defined by $x' = \frac{dx}{dz} = \frac{\dot{x}}{\dot{z}} \approx \frac{P_x}{P_z}$. Trace space is defined by the position and the slope of the particle trajectory moving along the direction of beam propagation; each particle has a point in x–x' space. The area occupied by all the points representing the particles in the beam form an area given by

$$A_x = \iint dx dx'. \tag{5.1}$$

The area of the beam in trace space is related to the definition of beam emittance. It is tempting to define the trace–space area as the beam emittance; however, it does. Defining A_x to be beam emittance does not distinguish between a laminar beam in a linear focusing system and a beam with the same trace space area but a distorted shape due to nonlinear forces and aberrations in the focusing lenses. The definition that follows for beam

emittance is presented in [23] in order to measure beam quality rather than trace–space area. Beam emittance needs to measure beam quality which we define as the product of the beam's width and its divergence. Divergence is related to the random velocity spread. To define an *rms emittance* $\tilde{\epsilon}_x$ quantity, we use moments of the distribution function. More information on moments can be found in Chapter 4. The rms emittance $\tilde{\epsilon}_x$ is given by

$$\tilde{\epsilon}_x = \Big(\langle x^2\rangle\langle x'^2\rangle - \langle xx'^2\rangle\Big)^{1/2} = \tilde{x}\frac{\tilde{v}_{x,th}}{v_0}. \tag{5.2}$$

The term $\langle xx'^2\rangle$ represents a relationship that exists between x and x' when the beam is either converging or diverging and is zero at the waist of a uniform beam. $\tilde{v}_{x,th}$ represents the x–component of the random kinetic energy, or equivalently, the rms velocity spread, and $\tilde{x} = \langle x^2\rangle^{1/2}$ is the x–component of the rms beam width. Using this definition, beam emittance, $\tilde{\epsilon_x}$, does increase when the beam passes through nonlinear focusing lenses even though the area A_x of the trace–space ellipse remains constant (which it must by Liouville's theorem [29]). As a special case, in a system where all forces acting on the particles are linear, the trace space area A_x is elliptical in shape, and if the ellipse is upright, having x_m and $(x')_m$ being the major and minor axes, the area of the ellipse is given by:

$$A_x = x_m(x')_m\pi \text{ and } \epsilon_x = x_m(x')_m = \frac{A_x}{\pi} \tag{5.3}$$

where $(x')_m$ denotes the maximum value of the divergence x' and not the slope of the width $\frac{dx_m}{dz}$. The definition $\epsilon_x = \frac{A_x}{\pi}$ also applies if the ellipse is tilted and is very useful for systems where the forces are linear.

The rms emittance gives very important quantitative information about the particle beam. A more useful measure of the beam quality is then defined as the effective emittance ϵ_{eff} which is generally expressed as:

$$\epsilon_{eff} = k_\epsilon\epsilon_{rms}, \tag{5.4}$$

where k_ϵ is a constant of proportionality which can change with the particle density distribution. For a beam with a uniform particle density distribution, or a K–V distribution, the relationship between the rms quantities $\tilde{\epsilon}_x$, $\tilde{x}$, and $\tilde{x}'_{th}$ and the effective quantities ϵ_{eff},

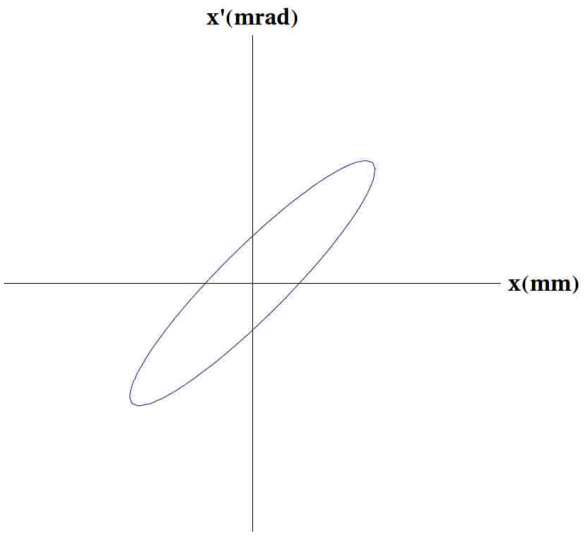

Figure 5.1: Trace–space ellipse used to understand beam quality or emittance.

x_m, and $(x')_m$ are given by

$$x_m = 2\tilde{x}, \tag{5.5}$$

$$(x')_m = 2\tilde{x}'_{th}, \tag{5.6}$$

and

$$\epsilon_{eff} = 4\tilde{\epsilon}_x. \tag{5.7}$$

Then, for a K–V distribution, $k_\epsilon = 4$, which is often referred to as the *four-times-rms-emittance*. The last definition of emittance, which is essential for comparing emittances from beams of different energies, is the effective normalized emittance $\epsilon_n = \gamma\beta\epsilon_{eff}$.

The beam width, whether *rms* or not, has units of meters, and the beam divergence has units of radians; therefore the units of measurement for emittance are m-rad. However since the quantities measures are typically on the order of millimeters and milliradians, it is customary to use units of mm-mrad as shown in Fig. 5.1. Many of the authors who define the emittance as the trace–space area of the beam A_x will include the factor of π either implicitly or explicitly, defining emittance as either $\epsilon_x = A_x$, or $\epsilon_x\pi = A_x$, and include π in the units, e.g., $\epsilon_x = 20\pi$ mm-mrad.

In the case of the beam with two-plane symmetry traveling along the z–axis, a complete description of the beam requires the beam width y_m, the divergence, $(y')_m$, and the effective emittance ϵ_y. If the beam is not continuous, but rather is bunched, i.e. the length of the beam is comparable to its diameter, longitudinal phase-space properties must be considered, which we neglect here.

5.2 Emittance for High Frequency TWTs

Usually, in vacuum-electronics, the electron beams employed have negligible emittance and are considered space–charge dominated. Increasingly, linear RF amplifiers are operating in frequency regimes where emittance is no longer negligible. Specifically, if we look again at the envelope equation introduced in Chapter 1 as Eq. 1.4:

$$r''[s] + \kappa[s] - \frac{2K_0}{r[s]^2} - \frac{\epsilon_{eff}}{r[s]^3} = 0,$$

where ϵ_{eff} is the effective emittance defined above. The emittance term scales as $\frac{1}{r^3}$ and so as the beam radius gets smaller as in devices operating at millimeter, submillimeter, and terahertz frequencies, the emittance term becomes increasingly important. We define a threshold emittance ϵ_{thr} as the emittance quantity which makes the space–charge term equal to the emittance term, e.g.

$$\frac{2K_0}{r[s]^2} = \frac{\epsilon_{thr}}{r[s]^3} \text{ or } \epsilon_{thr} = 2K_0 r[s]. \tag{5.8}$$

It is known that emittance growth can be expected from a variety of sources, including space–charge fields for beams with non-uniform current density profiles, and from applied

magnetic fields that vary nonlinearly with radius, as in a PPM field. However, over the typical length of an RF circuit, and for the types of beams common to RF amplifiers, emittance growth from these causes has not been observed appreciably in simulations, at least to the accuracy of the calculations within a few percent [28], [30].

It is, however, of great interest to have an analytic model which will give information about the emittance growth due to PPM focusing as devices are being built which employ beams that are on the limit between being space–charge and emittance dominated. The dominant forces in the electron beam define many of the device parameters and force different design choices for the amplifier from beam capture, confinement, and propagation. High emittance electron guns, particularly gridded guns, are also being used in high frequency amplifier design [31], and with a high initial emittance, a small emittance growth will have a much larger effect on device performance. The next section of this chapter is dedicated to quantifying emittance growth from PPM focusing as an important parameter for limitations in the design of high-frequency amplifiers.

5.3 Analytic Emittance Growth Calculations

In 1936, Scherzer showed that higher order radial terms always add in cylindrical magnetic lenses, leading to an unavoidable aberration in electron microscopes that limit resolution to 50 to 100 wavelengths which, for us, causes emittance growth [11]. This is known as Scherzer's Theorem, and we will evaluate its effect for the PPM model we developed earlier. It is also important to note that Scherzer, in 1947, showed that multipoles could be used to eliminate this aberration and that focusing using only multipoles could be aberration free [32].

For this calculation, we begin with electrons that are fixed in radius and have zero initial divergence traversing a PPM stack. These particles accumulate radial focusing as they go through the magnetic field. The linear part of the focusing is exactly cancelled by an equivalent space-charge force, but the residual non-linear part of the focusing leads to a

curvature in phase space. Because this geometry has radial symmetry, it is most convenient to calculate the resulting emittance growth using the particles' radial coordinate. We will calculate the emittance growth per unit length as a useful tool for understanding the emittance growth due to PPM fields over the length of an RF circuit.

The change in radial divergence after passing through an axial length is then

$$\Delta r'(r) = \frac{e}{mc\gamma\beta}^2 \left[\frac{B_z(r,z)\Delta z}{r} \int_0^r B_z(\rho,z)\rho d\rho + \frac{1}{r^3} \int_0^r B_z(\rho,z)\rho d\rho \int_o^r B_z(\rho,z)\rho d\rho \right], \quad (5.9)$$

where the magnetic field is found from the second order expansion of the field on–axis from

$$B_z(r,z) = B_0(z) - \frac{r^2}{4} B_0''(z). \quad (5.10)$$

If we assume the electrons are in laminar flow, we can calculate the emittance. Assume the field is periodic:

$$B_0(z) = B_p \cos(k_w z), \quad (5.11)$$

where $k_w = \frac{2\pi}{L}$ and where L is the magnet period. Expanding to second order, the field everywhere is then

$$B_z(r,z) = B_p \left(1 + \frac{k_w^2 r^2}{4} \right) \cos(k_w z). \quad (5.12)$$

Integrating we obtain

$$\int_0^r B_z(\rho,z)\rho d\rho = B_p \left(\frac{r^2}{2} + \frac{k_w^2 r^4}{16} \right) cos(k_w z), \quad (5.13)$$

and

$$\Delta r'(r) = -\Delta z \left(\frac{e}{2mc\gamma\beta}\right)^2 r B_p^2 \left(1 + \frac{k_w^2 r^2}{2}\right) \cos^2(k_w z). \tag{5.14}$$

Averaging over some distance, we have

$$\Delta r'_{ave}(r) = -\Delta z \left(\frac{e}{2mc\gamma\beta}\right)^2 r \frac{B_p^2}{2} \left(1 + \frac{k_w^2 r^2}{2}\right). \tag{5.15}$$

It is worth noting that if the field is decomposed into harmonics as

$$B_0(z) = \sum_{n=1}^{\infty} B_n \cos(n k_w z), \tag{5.16}$$

the induced convergence from the focusing is

$$\Delta r'_{ave}(r) = -\Delta z \left(\frac{e}{2mc\gamma\beta}\right)^2 \frac{r}{2} \sum_{n=1}^{\infty} B_n^2 \left(1 + n^2 \frac{k_w^2 r^2}{2}\right), \tag{5.17}$$

which is due to the orthogonality of the Fourier expansion. Keeping terms only to third order in radius is consistent with Scherzer's Theorem.

Now it is possible to calculate the emittance growth from the fundamental Fourier component of the axial magnetic field ($n = 1$). Note that it does not matter how this field is generated, the emittance growth will be the same. Moreover, since the fundamental component of the field is chosen to provide balanced flow for some given current, any PPM lattice that is designed for the same given current will lead to the same emittance growth. Therefore, henceforth we can use the transportable current as the design parameter. If the current is beyond the transport limit of the PPM structure it does not make sense to discuss emittance growth.

For balanced flow, the linear part of the induced convergence cancels the space-charge repulsion, which is linear if the beam is laminar and uniform. The emittance growth over a distance is then due to the nonlinear extra convergence, or

$$\Delta r'_{ave}(r) = -\Delta z \left(\frac{eB_p k_w}{4mc\gamma\beta}\right)^2 r^3. \tag{5.18}$$

With the following rms quantities:

$$\langle r^2\rangle = \frac{r_a^2}{2}, \quad \langle r'^2\rangle = \Delta z^2 \left(\frac{eB_p k_w}{4mc\gamma\beta}\right)^4 \frac{r_a^6}{4}, \quad \langle rr'\rangle = -\Delta z \left(\frac{eB_p k_w}{4mc\gamma\beta}\right)^2 \frac{r_a^4}{3}, \tag{5.19}$$

where r_b is the beam radius, the change in emittance is

$$(\Delta\epsilon_{norm})^2 = \frac{1}{4}\gamma^2\beta^2\left(\langle r^2\rangle\langle r'^2\rangle - \langle rr'\rangle^2\right) = \frac{1}{4}\gamma^2\beta^2(\Delta z)^2\left(\frac{eB_p k_w}{4mc\gamma\beta}\right)^4 \frac{r_a^8}{72}, \tag{5.20}$$

or

$$\Delta\epsilon_{norm} = r_a^4 \frac{\gamma\beta}{12\sqrt{2}}\left(\frac{eB_p k_w}{4mc\gamma\beta}\right)^2 \Delta z. \tag{5.21}$$

To understand the effect of emittance growth we consider the axisymmetric envelope equation:

$$r''[s] = \left(\frac{I/I_A}{\beta^3\gamma^3}\frac{1}{r[s]^2} - \left(\frac{eB_{rms}}{2mc\beta\gamma}\right)^2\right) r[s] + \frac{4\epsilon_{norm}^2}{\beta^2\gamma^2 r[s]^3}. \tag{5.22}$$

Equating the focusing term with the space–charge term,

$$r_a^2\left(\frac{eB_p}{4mc\gamma\beta}\right)^2 = \frac{I/I_A}{\beta^3\gamma^3}, \tag{5.23}$$

we can rewrite the emittance growth for the case of balanced laminar flow as in a PPM focused beam as

$$\Delta\epsilon_{norm} = \frac{r_a^2 k_w^2 (I/I_A)}{12\sqrt{2}\gamma^2\beta^2}\Delta z. \tag{5.24}$$

Equation 5.24 is our main result for emittance growth with PPM focusing. For the emittance term to equal the space-charge term, (what we define as the threshold emittance ϵ_{thres}) the following condition must be met:

$$\epsilon_{norm,thres} = r_a\sqrt{\frac{I}{I_A}\frac{1}{8\gamma\beta}}. \tag{5.25}$$

These last two equations can be combined to calculate what length of PPM structure is needed for the emittance grow to equal the space–charge term in the envelope equation, what we previously defined as the threshold emittance. This is a first order calculation to provide an estimate as the emittance actually increases, the field strength would have to be increased accordingly with an associated increase in the emittance growth rate:

$$\Delta z_{thres} = \frac{L^2}{r_a}\frac{3}{2\pi^2}\frac{(\gamma\beta)^{3/2}}{\sqrt{I/I_A}}. \tag{5.26}$$

It is illustrative to consider a few different cases, a higher energy case with longer period and a lower energy case with shorter period. First, a traditional PPM focused beam that is commonly found in TWTs would have an energy of 20 keV employing a PPM focusing lattice with an inner magnet radius of 1.25 cm and a sufficiently large outer radius to reach the asymptotic field. The maximum current density transportable by this PPM lattice is about 80 A/cm^2. The corresponding beam radius for a 1 μP beam is about 1.06 mm for a total current of 2.8 A. The threshold emittance is about 9.1 μm-mrad and the emittance growth rate is about 9.0 μm-mrad/m. Thus, the emittance does not begin to dominate the

beam dynamics and transport until about a meter of drift. This would be unusually long for an RF circuit and the emittance growth is a non–issue in devices like these.

For another case, we consider beam and lattice parameters for a 17 keV, Ka-band TWT device with an inner PPM magnet radius of 7 mm and an outer radius of 14 mm. The maximum beam current density is about 135 A/cm^2 therefore, the beam current is about 2.8 A with a beam radius of 0.81 mm, i.e. a perveance of about 1.26 μP. Here, the threshold emittance is about 5.5 μm-mrad with an emittance growth rate of about 8.4 μm-mrad/m, so the emittance growth becomes important for transport of the beam on the order of 1/2 meter.

An extreme extension of this case is to consider a 2.5 mm beam radius at the same energy, suitable for use in a 30 GHz tube (with a 1-cm RF wavelength). This beam would have a current of 26.5 A, i.e. an extreme 12 μP beam. The threshold emittance scales as the radius squared if the current density is held constant; therefore, the increase in current and radius now gives a threshold emittance of 68 μm-mrad, but the emittance growth rate, which scales as the radius to the fourth power, has increased even more, to 1310 μm-mrad/m. For this extreme case, the emittance growth will dominate the transport after only 5 cm.

It is clear to see from this analysis that most beams for RF interactions will not need to worry about emittance growth. It is, however, a very useful tool for calculating the threshold emittance for design considerations of RF tubes that are using more extreme electron beams, particularly beams of high perveance and beams of very small radii for high frequency amplifiers.

It is impossible to analytically calculate an emittance growth due to PMQ focusing, which is theoretically zero. With robust magnet models however, a beam code like MICHELLE should be able to calculate the emittance growth due to a PPM lattice and demonstrate a similar beam transport length with PMQ fields that have no emittance growth.

Chapter 6

Other PMQ Applications

6.1 Focusing Other Geometries

Another method for meeting the need for high current density electron beams for terahertz frequency devices is to use sheet beam geometry. There is currently much research in the area of sheet-beam amplifiers and sheet beam electron guns [31]. Options for beam transport for these devices is similar to the options for the pencil beam, namely, solenoidal, PPM, and PMQ. Solenoidal focusing of sheet beams is only possible for short transport distances as the diocotron instability affects longer distance transport [33]. There have been a few instances of using a version of PPM focusing to transport electron sheet beams [34], [35], [36]. It is of interest to see if PMQ could provide a more compact method of transport for sheet beams. Recent work by Wang et. al. [37] suggested a nonsymmetric quadrupole field for stable sheet beam transport. The conditions for stable sheet beam transport are presented in their article. We had performed multiple simulations to determine if a sheet beam could be transported using symmetric quadrupoles but with different spacing between the focus and defocus cells but were unable to support stable beam transport. Nonetheless, PMQs are a viable option for transporting electron sheet beams in a more compact way while transporting high current densities.

6.2 Metamaterial TWTs

The University of New Mexico (UNM) is currently part of a MURI program to develop metamaterial TWTs. In a metamaterial TWT, the slow wave structure is replaced by a novel electromagnetic interaction structure based on metamaterial properties [38]. TWTs will be explained in the following subsection, followed by an explanation of how PMQ focusing can be used to advantage with them. Among UNM's MURI partners, UC Irvine and Ohio State are both studying structures with degenerative band–edge modes and frozen modes. MIT is studying complementary split ring resonator structures like that pictured in Fig. 6.1.

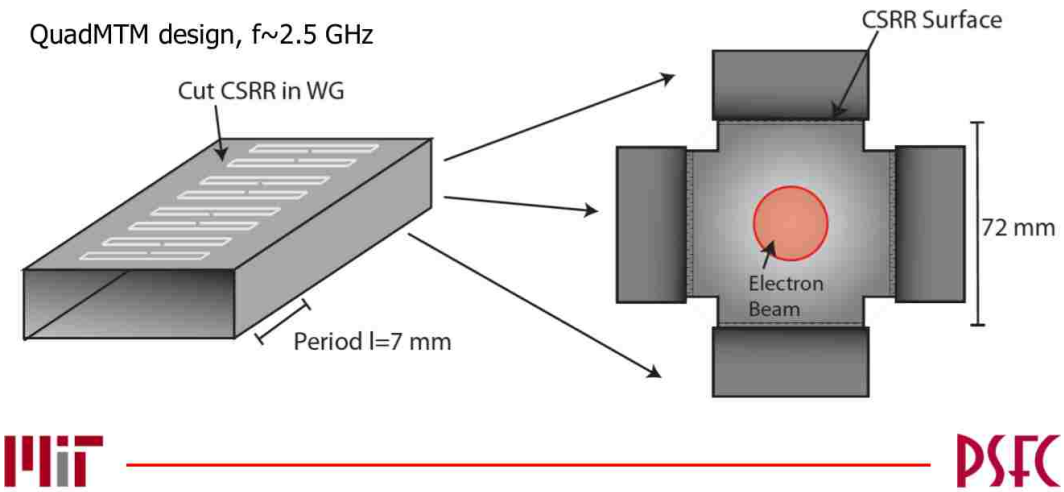

Figure 6.1: Novel interaction structure by researchers at MIT [4].

Due to the ability to transport relatively high current densities using PMQ lattices with lower occupancy, free space is left between the magnets. With PPM magnet lattices there is no free space in the lattice, even when the magnets are less than half the lattice period. In addition, pole pieces are required to smooth the fields between magnets and minimize field leakage. Pole pieces are not required in quadrupole focusing due to the transverse nature of the fields. These free space spaces in the focusing lattice are unique to PMQ focusing for space–charge dominated beams. We believe they could prove very useful for studying new novel electromagnetic structures because they allow for probes and other

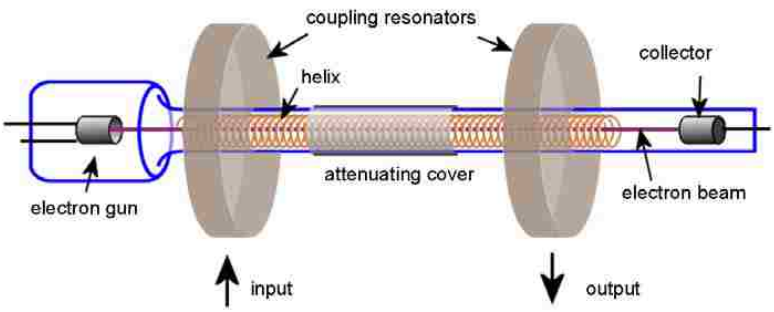

Figure 6.2: Typical TWT - helix variety [5].

diagnostics to be easily put into the interaction space between magnets in the lattice. This is a very attractive feature for experimentalists.

6.2.1 TWTs

Traveling–wave tubes are microwave and millimeter wave devices that utilize an electromagnetic field and particle beam interaction to slow down electrons, drawing kinetic energy out of the electrons and transferring it into RF energy. The strongest interaction between the field and the beam occurs when their velocities are equal, since electromagnetic fields typically travel at velocities near the speed of light, the longitudinal component of the field has to be slowed down to a velocity that is achievable for the electron beam. This is done by forcing the field to travel down a periodic structure which splits the field velocity into a transverse and a longitudinal velocity component. The periodic structure is aptly called the slow–wave structure (SWS) and is traditionally either a helix or a coupled–cavity structure. The helix structure is frequently used for lower power devices since higher powers can warp the helix structure, a typical helix TWT is pictured in Fig. 6.2. For higher–power handling TWTs, coupled-cavities are the SWS of choice. The process of converting electron energy into RF energy is stable, robust, and operates at a range of temperatures in which solid–state devices cannot operate.

TWTs are amplifiers and are used extensively for satellite communication due to their

temperature insensitivity, and are frequently used for military radar as well. The electromagnetic field profile in these devices is crucial, as the strength of the coupling between the field and the electron beam determines the gain of the device. Computer simulations play an important role in determining the performance of these devices as well as in studying physical phenomena inside the device. Simulations which can calculate both the fields and the charged particle motion theoretically provide a complete description of the electromagnetic fields.

Beam focusing was demonstrated through the envelope codes. In order to analyze the focused beam interaction with RF fields, a more computationally intensive simulation is required. Three dimensional simulation codes to predict electromagnetic field behavior, and particle behavior as the electrons interact with the fields, have proven to be very useful for studying physical phenomena and for determining the performance of the TWT device in question. It is important to determine whether or not the exotic beam profile of the PMQ focused electron beam will have an effect on the beam-field interactions inside a TWT. Work by NRL in 2009 [2], performed TWT simulations in the coupled-cavity TWT simulation code CHRISTINE and determined a relative insensitivity to beam radius by achieving similar gain (within 5 dB) for a TWT device with beams of the minimum and maximum radii of the PMQ focused beam. These are good results but we wanted to determine how the RF interaction and especially the space–charge bunching of the beam would be affected by the unique beam profile.

Simulations were performed using a fully electromagnetic finite–difference–time–domain particle-in-cell code which solves both Maxwell's equations and Newton's equations of motion at each time step. The code used is ICEPIC, developed and maintained by the Air Force Research Laboratory at Kirtland Air Force Base [39]. This code allows us to fully simulate the interaction of the electron beam with the RF fields in an amplifying structure, such as the TWT. For this simulation, a coupled–cavity TWT structure is chosen which operates in the Ka-band, around 35 GHz. The device geometry can be pictured in Fig. 6.3, and detailed dimensions can be found in [40]. This particular coupled–cavity TWT is chosen for ease of manufacturing, ease of simulation geometry, and scalability to

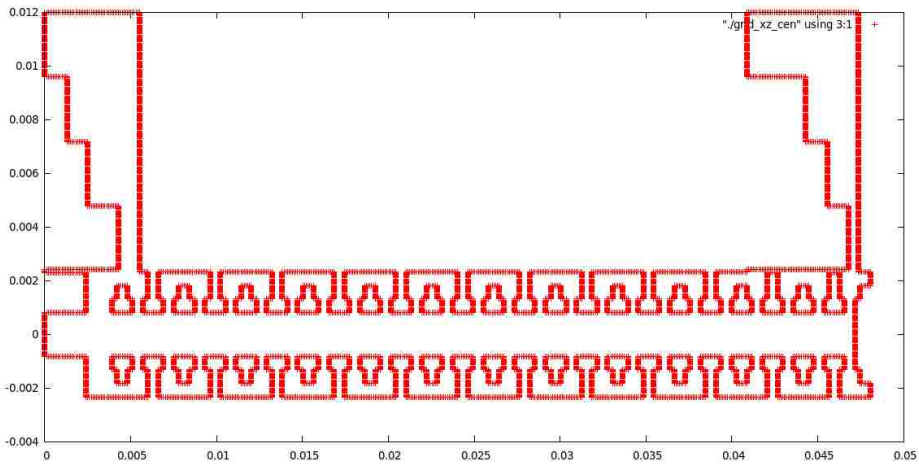

Figure 6.3: Cross-sectional view of the double-slot coupled cavity SWS circuit.

higher frequencies. Accurate representations of the electromagnetic fields and the charged particle, in this case the electron beam, are required to determine device performance.

To study this, a coupled-cavity TWT structure was chosen to be simulated with the PMQ focused electron beam. The intention was to import the magnet simulations from Maxwell into ICEPIC. We were able to import the magnetic field, but the resolution of the magnet simulations was limited by computer memory and we observed non–uniformity in the imported fields, similar to the anomalies described in Chapter 3. This non–uniformity prevented successful transport in ICEPIC. It is believed that successful transport will not be achieved without more robust magnetic field simulations, or an analytic analytic off-axis expansion of the quadrupole field such that the ideal fields can be calculated on a grid for importing into ICEPIC or a similar code. The magnetic field loops inherent to ICEPIC are insufficient to construct the dual-plane symmetry of the quadrupole field lattice. We believe that the periodicity of the magnet lattice could have an effect on the RF–beam interaction as in PPM focusing. Due to the inability to successfully transport the beam, TWT simulations are suggested as future work that can better explore the effects of PMQ focusing both on beam-wave interaction and on emittance growth.

Chapter 7

Conclusions and Future Work

A full analytic study of the magnetic fields due to PPM and PMQ focusing lattices has been performed especially to the end of developing thorough envelope codes for space–charge dominated electron beam transport. Envelope codes were developed and analyzed for different magnet parameters and different beam parameters. Using these envelope codes, a full analysis and comparison between the compact confining methods using PPM and PMQ lattices was performed with full parameter studies to show the limitations of each method depending on magnet parameters and beam voltage. An optimization method was developed for determining the maximum transportable current density per period S. It was determined that PMQ focusing can transport relatively high current densities; however, it is not an advantage over PPM focusing as was suggested by previous work. The advantageous region of transportable current density suggested by the analytic model disappeared when accurate magnet models were used. Figure 7.1, previously shown in Chapters 1 and 4, respectively, demonstrates this clearly.

The actual advantages of using PMQs over PPMs is due to their lower occupancy and to the elimination of emittance growth. Lower occupancy decreases the cost and weight of the magnetic material required to transport a comparable beam to PPM focusing. The analytic emittance growth due to the nonlinear fields in PPM lattices was calculated; this is

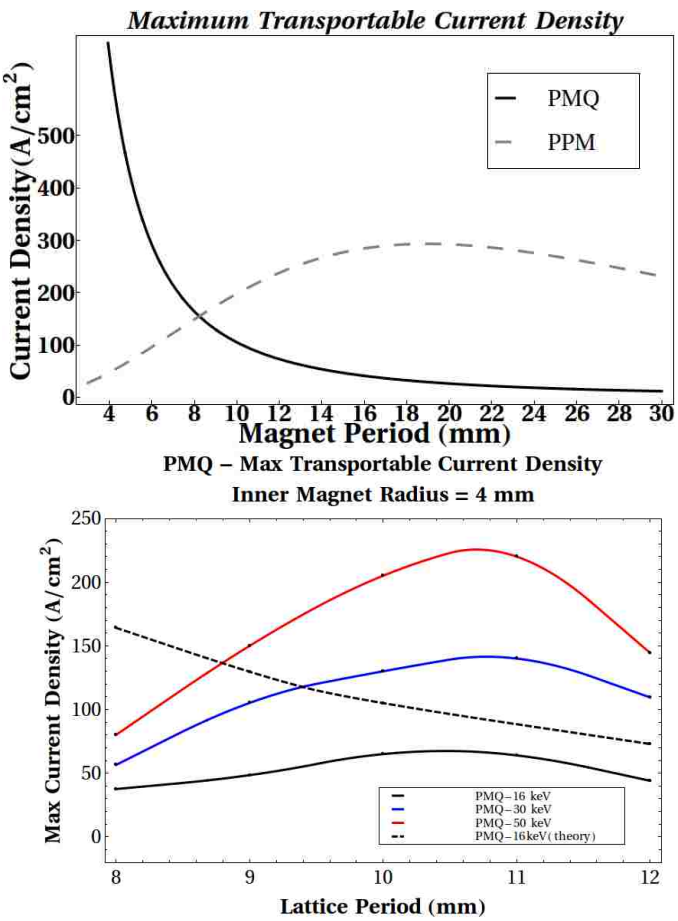

Figure 7.1: Maximum transportable current density per lattice period from Eqs. 1.5 and 1.6, top, and from envelope code calculations, bottom.

an important tool for determining design parameters for more extreme electron beams with higher perveance, higher initial emittance, and smaller areas. The advantage of eliminating emittance growth will become a factor as we move towards more extreme beams to achieve the power levels and performance requirements at terahertz frequencies.

Further study should be performed of very high fidelity simulations of the RF interaction with the exotic true beam profile of the PMQ focused beam to ensure the space–charge bunching of the beam remains stable. Theoretically, it is likely the PMQ profile will interact properly with the RF field since, in the case of PPM focused beams, the changing

radius in the profile of the beam does not affect the space–charge bunching of the beam. We also know from previous work that the beam–wave interaction is relatively insensitive to the percentage of radial variation over the PMQ focused beam.

Further work is also needed to verify though computer simulations the analytic proof of emittance growth through PPM focusing lattices as well as to verify the theoretical zero-emittance growth of beams traversing PMQ lattices. This will require high performance computing to achieve the accuracy needed.

References

[1] J.T. Mendel, C.F. Quate, and W.H. Yocum. Electron beam focusing with periodic permanent magnet fields. *Proc. of the IRE*, 42(5):800–810.

[2] D.K. Abe, R.A. Kishek, J.J. Petillo, D.P. Chernin, and B. Levush. Periodic permanent-magnet quadrupole focusing lattices for linear electron-beam amplifier applications. *IEEE Trans. Electron Dev.*, 56:965–973, 2009.

[3] K. Halbach. *NIM*, (1), 1980.

[4] J.S. Hummelt, S. Lewis, M. Shapiro, and R.J. Tempkin. Design of a metamaterial-based backward-wave-oscillator. *IEEE Trans. Plasma Science*, 42(4):903–936, 4 2014.

[5] C. Wolff. Available: http://www.radartutorial.eu/08.transmitters/travelingtext available under the GNU Free Documentation License.

[6] K. Nichols, B. Carlsten, and E. Schamiloglu. Analysis of quadrupole focusing lattices for electron beam transport in traveling-wave tubes. *IEEE Trans. Electron Devices*, 61(6):1865–1870, 6.

[7] J.R. Pierce. *Theory and Design of Electon Beams.* Van Nostrand, 2 edition, 1954. Princeton, NJ.

[8] L. Brillouin. A theorem of larmor and its importance for electrons in magnetic fields. *Phys. Rev.*, 107(7-8):260–266, 1945.

[9] C.M. Armstrong. The truth about terahertz. *IEEE Spectrum*, 49(9):36–41.

[10] K.L. Jensen. Electron emission physics. *Advances in Imaging and Electron Physics*, 149.

[11] O. Scherzer. Über einige fehler von elektonenlinsen. *Seitshrift für Physik*, 101(9).

[12] T. Wessel-Berg. A new quadrupole ppm focusing scheme for high density electron beams. *IEDM Tech. Dig.*, pages 153–156, 12 1993.

[13] Trace 3-d. Los Alamos National Laboratory, University of California, Available: http://laacg.lanl.gov/laacg/services/download_trace.phtml.

[14] J.J. Petillo, K. Eppley, D. Panagos, P. Blanchard, E. Nelson, N. Dionne, J. DeFord, B. Held, L. Chernyakova, W.j Krueger, S. Humphries, T. McClure, A. Mondelli, J. Burdette, M. Cattelino, R. True, K. T. Nguyen, and B. Levush. The michelle three-dimensional electron gun and collector modeling tool: Theory and design. *IEEE Trans. Plasma Sci.*, 30(3):1238–1264, 6 2002.

[15] Ansoft LLC. Maxwell 2d/3d electromagnetic field solver. Available: http://www.ansoft.com.

[16] D.P. Grote, A. Friedman, I. Haver, and S. Yu. Three-dimensional simulations of high current beams in induction accelerators with warp3d. *Fus. Eng. Des.*, 32-33:193–200.

[17] K. Halbach. Physical and optical properties of rare earth cobalt magnets. *Nucl. Instrum. Methods*, 169:109–117, 1981.

[18] B.N. Basu. *Electromagnetic Theory and Applications in Beam-Wave Electronics.* World Scientific Publishing Co., 1 edition, 1996.

[19] A.S. Gilmour. *Klystrons, Traveling-Wave-Tubes, Magnetrons, Crossed-Field Amplifiers, and Gyrotrons.* Artech House, Norwood, MA, 1 edition, 2011.

[20] J.E Sterrett and H. Heffner. The design of periodic magnetic focusing structures. *IRE Trans. Electron Devices*, 5.

[21] J.B. Rosenzweig. Analysis of halbach segmented pure permanent magnet quadrupole. Master's thesis, UCLA, Department of Physics and Astronomy, 2004. http://pbpl.physics,ucla,edu/Education/Talks/HalbachPMQ.pdf.

[22] R. Kishek. private communications, 2012, 2013.

[23] M. Reiser. *Theory and Design of Charged Particle Beams.* Wiley-VCH Verlag, Weinheim, Germany, 2008.

[24] J.D. Lawson. *The Physics of Charged Particle Beams.* Oxford University Press, 2 edition, 1988.

[25] I.M. Kapchinsky and V.V. Vladimirsky. Limitations of proton beam current in a strong focusing linear accelerator associated with beam space charge. *Proc. Int. Conf. High Energy Accel.*, pages 274–288, 1959. Geneva, Switzerland.

[26] IL Wolfram Research, Champaign. Wolfram mathematica 8. Available: http://www.wolfram.com/mathematica.

[27] J.J. Petillo, E.M. Nelson, J. F. DeFord, N. J. Dionne, and B. Levush. Recent developments to the michelle 2-d/3-d electron gun and collector. *IEEE Trans. Electron Devices*, 52(5):742–748, 5 2005.

[28] D.R. Whaley. Practicle design of emittance dominated linear beams for rf amplifiers. *IEEE Trans. Electron Devices*, 61(6):1726–1734, 6 2014.

[29] J. Liouville. Sur les deux derniers cahiers du journal de m. crelle. *Journ. de Math.*, 3:1–3, 1838.

[30] R. True. Emittance and the design of beam formation, transport, and collection systems in periodically focussed twts. *IEEE Trans. Electron Devices*, 34(2):473–485, 2 1987.

[31] A. Strivastava, J.K. So, and G.S. Park. Development of high current density sheet beam electron gun for terahertz devices. In *10.3, 2008 IEEE International Vacuum Electronics Conference*, 2008.

[32] O. Scherzer. Sparische und chromatische korrektur von elektonenlinsen. *Optik*, 2:114–132, 1947.

[33] J. Booske, B.D. McVey, and T.M. Antonson. Stability and confinement of nonrelativistic sheet electron beams with periodic cusped magnetic focusing. *J. Appl. Phys.*, 73(9):4140–4155, 5 1993.

[34] J.-X. Wang, L.R. Barnett, N.C Luhmann, Y.-M. Shin, and S. Humphries. Electron beam transport analysis of w-band sheet beam klystron. *Physics of Plasmas*, 17, 2010. 043111.

[35] B.E. Carlsten. *Phys. Plasmas*, (9), 2002. 5088.

[36] B.E. Carlsten, L.M. Earley, F.L. Krawczyk, S.J. Russell, J.M. Potter, P. Ferguson, and S. Humphries. *Phys. Rev. St Accel. Beams*, 8 062001, 2005.

[37] Z. Wang, Y. Gong, Z. Duan, H. Gong, Z. Lu, L. Yue, H. Yin, J. Xu, Y. Li, P. Liu, and G.S. Park. Stable sheet-beam transport in periodic nonsymmetric quadrupole field. *IEEE Trans. Plasma Science*, 38(1):32–38, 1 2010.

[38] T. Wynkoop, M. Gilmore, A.G. Lynn, S. Prasad, and E. Schamiloglu. Characterizing electrical and thermal breakdown of metamaterial structures of hpm applications. *Proc. IEEE PPS-2013*, 6 2013. San Francisco, CA.

[39] R.E. Peterkin and J.W. Luginsland. A virtual prototyping environment for directed energy concepts. *Comp. Sci. Eng.*, 4:42–48, 2002.

[40] H.J. Kim, H.J. Kim, and J.J. Choi. Magic3d simulations of a 500-w ka-band coupled-cavity traveling-wave-tube. *IEEE Trans. Electron Devices*, 56(1):149–154.